NUMERICAL IMPLEMENTATION OF A STRAIN GRADIENT PLASTICITY MODEL COUPLED WITH NONLOCAL DAMAGE

A THESIS SUBMITTED TO
THE GRADUATE SCHOOL OF NATURAL AND APPLIED SCIENCES
OF
MIDDLE EAST TECHNICAL UNIVERSITY

BY

İZZET ERKİN ÜNSAL

IN PARTIAL FULFILLMENT OF THE REQUIREMENTS
FOR
THE DEGREE OF MASTER OF SCIENCE
IN
AEROSPACE ENGINEERING

OCTOBER 2024

Approval of the thesis:

NUMERICAL IMPLEMENTATION OF A STRAIN GRADIENT PLASTICITY MODEL COUPLED WITH NONLOCAL DAMAGE

submitted by **İZZET ERKİN ÜNSAL** in partial fulfillment of the requirements for the degree of **Master of Science in Aerospace Engineering Department, Middle East Technical University** by,

Prof. Dr. Naci Emre Altun
Dean, Graduate School of **Natural and Applied Sciences** _____

Prof. Dr. Serkan Özgen
Head of Department, **Aerospace Engineering** _____

Assoc. Prof. Dr. Tuncay Yalçınkaya
Supervisor, **Aerospace Engineering, METU** _____

Examining Committee Members:

Assoc. Prof. Dr. Ercan Gürses
Aerospace Engineering, METU _____

Assoc. Prof. Dr. Tuncay Yalçınkaya
Aerospace Engineering, METU _____

Prof. Dr. Demirkan Çöker
Aerospace Engineering, METU _____

Assist. Prof. Dr. Görkem Eğemen Güloğlu
Aerospace Engineering, METU _____

Assist. Prof. Dr. Mehmet Okan Görtan
Mechanical Engineering, Hacettepe University _____

Date:07.10.2024

I hereby declare that all information in this document has been obtained and presented in accordance with academic rules and ethical conduct. I also declare that, as required by these rules and conduct, I have fully cited and referenced all material and results that are not original to this work.

Name, Surname: İzzet Erkin Ünsal

Signature :

ABSTRACT

NUMERICAL IMPLEMENTATION OF A STRAIN GRADIENT PLASTICITY MODEL COUPLED WITH NONLOCAL DAMAGE

Ünsal, İzzet Erkin
M.S., Department of Aerospace Engineering
Supervisor: Assoc. Prof. Dr. Tuncay Yalçınkaya

October 2024, 85 pages

This thesis presents the implementation of a lower-order strain gradient plasticity model to capture size-dependent plastic deformation and nonlocal damage effects. Two methods are employed to calculate the effective plastic strain gradient: the interpolation method, which uses plastic strain values at integration points, and the extrapolation method, which utilizes nodal values of plastic strain. The extrapolation method consistently predicts higher plastic strain gradients, leading to stronger material responses, particularly in cases involving sharp boundaries or material interfaces. However, both methods exhibit similar overall trends in simpler problems. The strain gradient framework is extended to include nonlocal damage effects through a volumetric averaging scheme. The interaction between hardening due to strain gradients and softening from damage is explored in several numerical simulations. Results indicate that increasing the damage length scale results in more diffused damage zones. In problems with sharp cracks, increasing the length scale associated with plasticity accelerated failure due to the intense strain gradients developing at the crack tip. Conversely, in problems with blunt cracks, the same length scale delayed failure by diffusing the localization of plastic deformation. Overall, the framework successfully

captures the complex mechanisms governing material failure, depending on both geometry and loading conditions. The incorporation of strain gradient and nonlocal damage effects provides a versatile tool for modeling size-dependent behavior and damage evolution.

Keywords: Strain gradient plasticity, Nonlocal damage, Size effect, CMSG theory

ÖZ

GERİNİM GRADYANI PLASTİSİTESİ İLE BİRLEŞTİRİLMİŞ BİR YEREL OLMAYAN HASAR MODELİNİN SAYISAL UYGULAMASI

Ünsal, İzzet Erkin
Yüksek Lisans, Havacılık ve Uzay Mühendisliği Bölümü
Tez Yöneticisi: Doç. Dr. Tuncay Yalçınkaya

Ekim 2024 , 85 sayfa

Bu tez, boyuta bağlı plastik deformasyon ve yerel olmayan hasar etkilerini yakalamak için düşük dereceli bir gerinim gradyan plastisite modelinin uygulanmasını sunmaktadır. Etkin plastik gerinim gradyanını hesaplamak için iki yöntem kullanılmıştır: integrasyon noktalarındaki plastik gerinim değerlerini kullanan interpolasyon yöntemi ve plastik gerinimin düğüm değerlerini kullanan ekstrapolasyon yöntemi. Ekstrapolasyon yöntemi, özellikle keskin sınırlar veya malzeme arayüzleri içeren durumlarda, daha güçlü malzeme tepkilerine yol açan daha yüksek plastik gerilme gradyanlarını tutarlı bir şekilde tahmin etmiştir. Bununla birlikte, her iki yöntem de daha basit problemlerde benzer genel eğilimler sergilemiştir. Gerinim gradyanı çerçevesi, hacimsel bir ortalama şeması aracılığıyla yerel olmayan hasar etkilerini içerecek şekilde genişletilmiştir. Gerinim gradyanlarından kaynaklanan sertleşme ile hasardan kaynaklanan yumuşama arasındaki etkileşim çeşitli sayısal simülasyonlarda incelenmiştir. Sonuçlar, hasar uzunluk ölçeğinin artmasının daha dağınık hasar bölgelerine yol açtığını göstermiştir. Keskin çatlakların olduğu problemlerde, plastisite ile ilişkili uzunluk ölçeğinin artırılması, çatlak ucunda gelişen yoğun gerinim gradyanları nedeniyle başa-

rısızlığı hızlandırmıştır. Buna karşılık, küt uçlu çatlaklı problemlerde, aynı uzunluk ölçeği plastik deformasyonun lokalizasyonunu dağıtarak kırılmayı geciktirmiştir. Genel olarak, çerçeve, hem geometriye hem de yükleme koşullarına bağlı olarak malzeme hasarını belirleyen karmaşık mekanizmaları başarılı bir şekilde yakalamaktadır. Gerinim gradyanı ve yerel olmayan hasar etkilerinin dahil edilmesi, boyuta bağlı davranış ve hasar gelişiminin modellenmesi için çok yönlü bir araç sağlamaktadır.

Anahtar Kelimeler: Gerinim gradyan plastisitesi, Yerel olmayan hasar, Boyut etkileri, CMSG teorisi

To my family

ACKNOWLEDGMENTS

First and foremost, I would like to express my deepest gratitude to my supervisor, Assoc. Prof. Dr. Tuncay Yalçınkaya, for his unwavering support, endless patience, and constant encouragement. His invaluable guidance and friendship have played a crucial role in the success of this thesis. His passion for research and commitment to excellence have been a continual source of inspiration. I am eternally grateful to him for being an exceptional role model throughout this journey.

I am also sincerely thankful to the members of my thesis committee—Assoc. Prof. Dr. Ercan Gürses, Prof. Dr. Demirkan Çöker, Assist. Prof. Dr. Görkem Eğemen Güloğlu, and Assist. Prof. Dr. Mehmet Okan Görtan—for their insightful feedback, patience, and support. Their expertise has significantly enriched the quality of this work.

A special thanks goes to my colleagues and friends in the Yalçınkaya Research Group for their companionship and collaboration, especially Hande Vural, Orhun Bulut, and Enes Günay, for the stimulating discussions and for making this journey more enjoyable. I would also like to extend my heartfelt thanks to Can Erdoğan, whose contributions, endless discussions, unwavering patience, and constant support have been invaluable.

I am deeply grateful to my closest friends, Murad İlhan, Yusuf Pekmezci, Özgür Yolasığmaz, Umut Baydar, Denizhan Aksoy and Berkehan Tatlı. Thank you all for always being there when I needed you most. Your friendship has meant the world to me, and I will forever be grateful for your support.

Above all, I am eternally indebted to my family for their unconditional love, patience, and belief in me. To my parents, Nefise and Şükrü, thank you for always encouraging me to pursue my dreams and for standing by my side through every challenge and triumph.

TABLE OF CONTENTS

LIST OF TABLES

TABLES

LIST OF FIGURES

FIGURES

CHAPTER 1

INTRODUCTION

It has been demonstrated through several tests that the mechanical response given by the metallic materials having a typical length scale of microns or submicrons exhibit a significant size effect. A series of static torsion and tensile tests conducted on copper wires with diameters ranging from 12 to 170 micrometers [1] as shown in Figure 1.1, indicate that smaller-diameter wires exhibit a significantly stiffer torsional response when normalized by wire radius. Conversely, tensile testing on the same samples have not shown significant size dependency. Similar experiment were performed and reached the same findings [2, 3].

Another observation from [1] is a pronounced size dependency in Vickers micro-indentation experiments, particularly in tests performed for single crystal tungsten samples. The studies have shown notable correlation between size and material hardness, as the hardness doubled when employing an indent with a diagonal that is ten times smaller. Several other researchers have also documented similar size effects in micro-indentation tests for various other metallic materials [4–8].

A similar tendency towards size reduction was also noted in the bending of ultra thin nickel foils. Most notably, micro-bending experiments [9] performed for thin nickel foils with thicknesses ranging from $12.5\,\mu\mathrm{m}$, $25\,\mu\mathrm{m}$, and up to $50\,\mu\mathrm{m}$. Their results highlighted in Figure 1.3 shows that thinner foils exhibited greater strength. Specifically, the normalized applied bending moment for the $50\,\mu\mathrm{m}$ thick foil was double the amount of that for the $12.5\,\mu\mathrm{m}$ foil. Comparable results were obtained by Ehrler et al. [10]. Additionally, for the tension and compression experiments performed on metal matrix composites, several studies have demonstrated that decreasing the particle size, while maintaining a constant particle volume fraction, significantly enhances

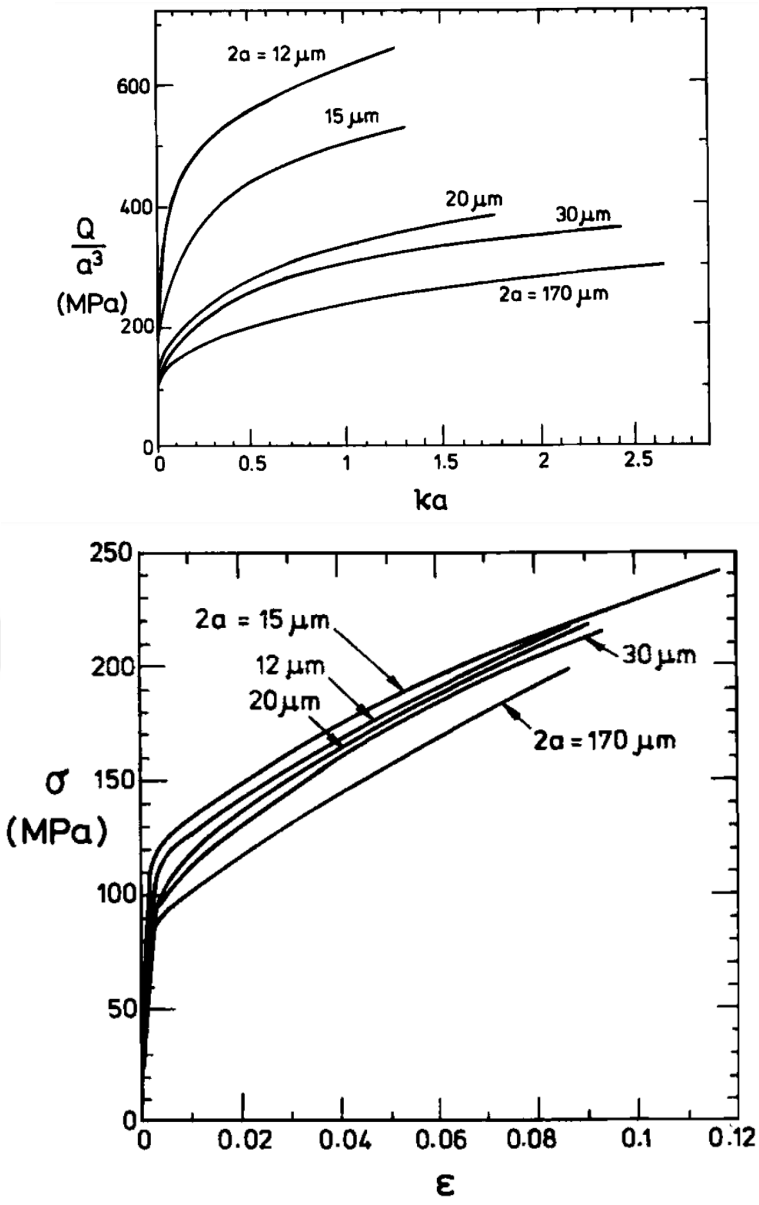

Figure 1.1: a) Torsional behavior of copper wires with diameters $2a$ ranging from $12\,\mu\mathrm{m}$ to $170\,\mu\mathrm{m}$. Q given as the torque, and κ given as the twist per unit lenght. Both are normalized by the wire radius a. b) σ versus ε under tensile loading: wire diameter has minimal impact on the response, based on [1].

the flow strength of the material [11–15].

Classical continuum plasticity theories cannot predict or explain these size-dependent effects in metals, as they do not incorporate internal length scales in their constitutive models. All solid materials inherently possess microstructures, such as crystal lat-

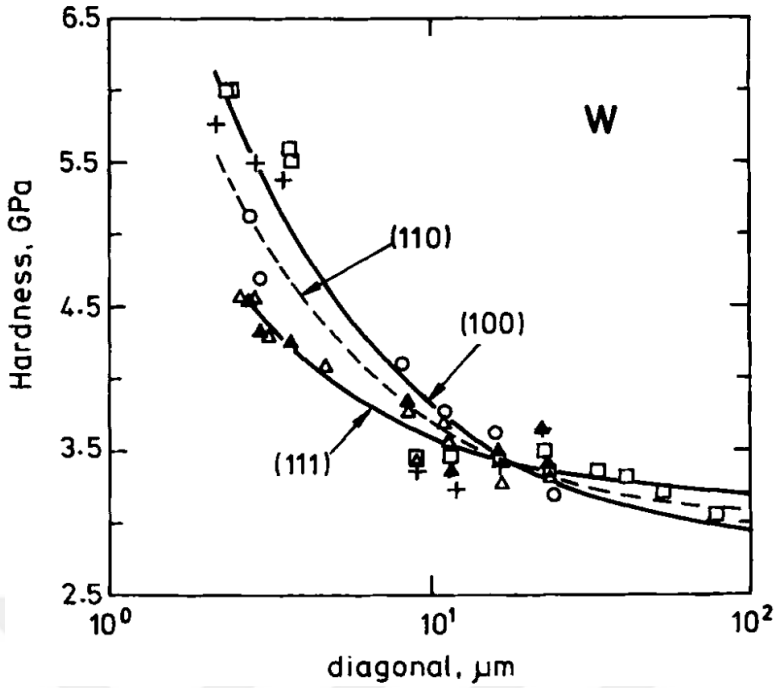

Figure 1.2: Influence of indent size on the hardness of tungsten single crystals, where the indent size is defined by the diagonal length of the Vickers micro-indenter, as reported in [5].

tices, inclusions, grains, and grain clusters. These microstructures require characteristic lengths to represent their size and influence on the material's behavior. Classical continuum mechanics determines the stress state based on the deformation history at a single material point, a method that suffices for many applications. However, the experiments mentioned above reveal size-dependent phenomena that classical plasticity theories fail to predict or explain. This difference underscores the necessity of incorporating characteristic lengths into material models to capture the impact of microstructures on their mechanical behavior. Therefore, a microscopic understanding of plasticity is becoming necessary to describe deformation at small length scales accurately. Deformation of material causes the development, migration, and storage of dislocations, which ultimately results in work hardening. Dislocations are stored in materials for two primary reasons: they either accumulate randomly by trapping one another, known as statistically stored dislocations (SSDs) [16], or they form to ensure compatible deformation between different regions of the material, referred to as geometrically necessary dislocations (GNDs) [16, 17]. Geometrically necessary

dislocations are associated with plastic shear gradients in the material. These plastic strain gradients develop due to the loading geometry or non-uniform deformation within the material. These considerations have motivated the development of strain gradient theories. Strain gradient theories were developed as an alternative approach, proposing that the stress at a point is influenced not only by the strain (the first derivative of the displacement field) but also by the strain gradient (the second derivative of the displacement field). Dimensional analysis reveals that, unlike strain, the strain gradient is not dimensionless and must be scaled by a characteristic length. This dimensional inconsistency enables strain gradient theories to capture size effects, as an internal length scale is inherently introduced to balance the dimensions of strain and strain gradient.

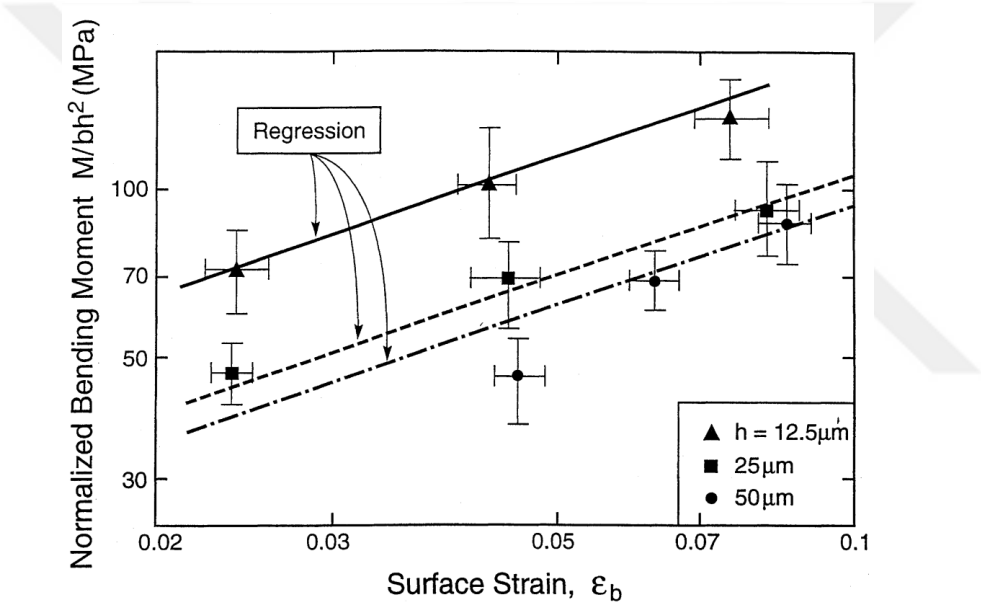

Figure 1.3: Variation of the normalized bending moment versus the surface strain for all three foil thicknesses, from [9].

A number of strain gradient frameworks have been proposed over the last two decades. In literature, strain gradient theories have been separated into two classes. The first class of strain gradient theories referred to as higher-order theories [1,18–22], initially proposed by [23], uses higher-order stress terms as the work conjugate to the strain gradient. Due to this, the equilibrium equations need to be adapted, and additional boundary conditions and tractions must be considered. The second class, known as lower-order SG theories [24–29], initially proposed by [30], involves the conventional

stress description, retains all of the features of classical plasticity theory and does not necessitate any additional higher-order boundary conditions. This class of strain gradient models incorporate the strain gradient effects only in the calculation of the flow strength of the material. Therefore, they do not require any change in the equilibrium equations, as only the hardening function of the material is modified. This feature of lower-order theories is what makes them easier to implement in a commercial finite element solver. However, some inaccuracies might be observed due to the lack of higher-order stress terms and additional boundary conditions, a notable example being the boundary layer phenomenon [18].

The high-order and lower-order theories of gradient plasticity have proven themselves to be effective in accurately predicting the mechanical response for different metallic materials in microscale, under various loading circumstances. Classical examples such as torsion in thin copper wire, or bending of extremely thin nickel foils [25, 31–33], micro- and nanoindentations [7, 34, 35], the void-size effect in microporous materials [36–38], size-dependent mechanical behaviors of metal matrix composites [28, 39–46], periodic flat punching to produce micron or submicron scale features [47–52], analysis of bulk metallic glasses and amorphous plasticity [53, 54] cleavage fracture near sharp crack tips [55–59], and size effects observed in single, bi or polycrystal metals [60–62].

Nevertheless, the strain gradient theories above do not consider the influence of microscopic damage in materials, which inevitably occurs during severe plastic deformation. The key processes behind ductile damage are commonly understood to include the initiation of voids (nucleation), their subsequent expansion (growth), and the eventual merging of these voids (coalescence). According to Continuum Damage Mechanics (CDM) [63], these mechanisms lead to the degradation of the material's mechanical characteristics, leading to strain-softening behavior and the formation of micro cracks. For instance, during the machining of titanium alloys, substantial material removal occurs through the generation of intense shear forces within localized regions known as shear bands (as illustrated in Figure 1.4). At high cutting speeds (up to $90\,\mathrm{m/s}$) [64–66], the shear bands are subjected to substantial strain rates (around $10^5\,\mathrm{s}^{-1}$) [67–69]. These extreme stresses and strains lead to plastic deformation, resulting in strain-softening of the material in those regions.

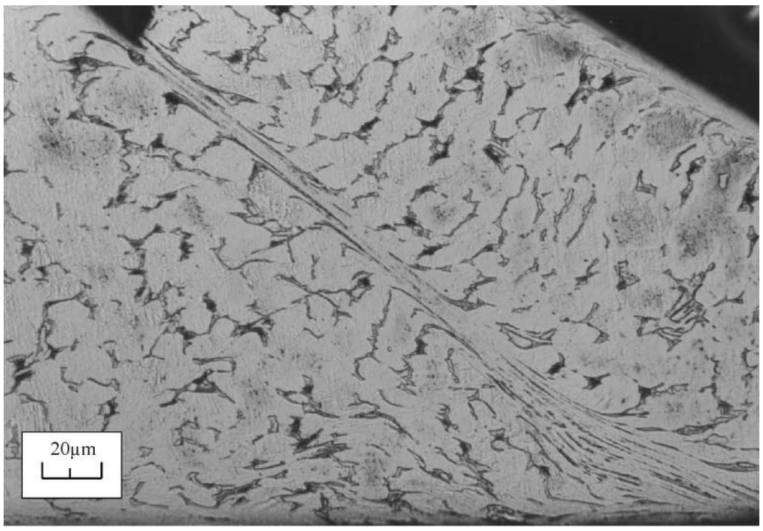

Figure 1.4: Formation of adiabatic shear bands in titanium alloy Ti-6Al-4V during orthogonal cutting at a velocity of $V = 13\,\mathrm{m/s}$, from [64].

To accurately capture strain softening phenomena, some strain gradient models have introduced a negative softening modulus. This approach is utilized to model shear-band localization and capture the softening behavior in ductile materials [70–74]. When the material experiences a reduction in flow stress (i.e., softening), the nonlinear plastic behavior modifies the governing partial differential equations of equilibrium. This alteration leads to a strong sensitivity to the mesh used, causing the solution to not converge to a stable value as the mesh size is reduced. This issue emerges because, in the softening regime, the negative material modulus causes the partial differential equilibrium equations to lose ellipticity [75–77]. One way to address this mesh dependency and recover stability is by employing a nonlocal regularization procedure.

To enhance a model with nonlocal regularization, two common approaches are used: gradient-type models that involve differential operators, and integral-type models that employ spatially weighted averages. These procedures often enhance the model equations to avoid the concentration of strain into a very small area, thereby acting as limiters for localization. Pioneering work in [78] provided an in-depth comparison of the regularization characteristics across various strain gradient theories. They examined the tensile response of a one-dimensional bar, focusing solely on softening plastic behavior. They assessed the regularization behavior of multiple theories, such

as the Toupin-Mindlin elastic strain gradient theory [79, 80], Chambon et al.'s plastic version of the Toupin-Mindlin theory [81], the plastic strain gradient theory by Fleck and Hutchinson [1], as well as the Mechanism-based strain gradient theory [82], were also examined. They further argue that in a broad sense, all models that involve some characteristic length scale and gradient terms can be classified as nonlocal.

This concept is based on the principle such that, in all gradient models, the gradient term can represent either strain gradients, which are work-conjugate to higher-order stresses in the equilibrium equations, or gradients of internal variables, which are linked to dissipative thermodynamic forces that influence the evolution equations but do not appear in the equilibrium (momentum balance) equations.

Nonetheless, for both models, a dependency on the immediate vicinity of the point is considered, thereby enforcing nonlocality. Drawing inspiration from this fact, many ductile damage models that use an internal variable for nonlocal regularization have been proposed in the literature. Nonlocal formulations have gained significant traction within the ductile damage community as a solution to the pathological mesh dependency inherent in local continuum models. The nonlocal continuum approach serves as a practical solution for regularizing boundary value problems that involve strain softening. It effectively captures size effects and prevents artificial localization, which can otherwise lead to mesh sensitivity in numerical analyses. In recent decades, numerous nonlocal models have been developed to tackle these challenges.

Following the efforts in [83], who were the first to apply a nonlocal continuum approach to ductile damage, and the advancements from [84] and [85], nonlocal models have since been widely adopted to address the regularization of strain-softening behavior in ductile materials. As an alternative approach phase field modeling has been used extensively to model nonlocal damage in applications such as forming and fatigue [86–89]. On the other hand, gradient type model termed as damage-enriched, [90, 91] have been developed and used which incorporate the damage field gradient, achieving a regularization effect similar to that found in strain gradient theories. [92] expanded this model by implementing the damage law, where the nonlocal variable is chosen as the equivalent plastic strain. Moreover, widely recognized damage models like the GTN model, initially proposed by [93] and subsequently refined

by [94] and [95], have been extensively applied in nonlocal damage modeling. In these models, porosity (void volume fraction) is typically treated as a localized variable (see e.g., [96–98]). Many other researchers have included the damage variable's gradient in their models to ensure solution regularization [99–101].

Some damage effects have been indirectly addressed within the framework of strain gradient theories. For example, [102] suggested that the intrinsic material length should vary with plastic deformation, rather than remain constant as assumed in many strain gradient models. Moreover, [103] demonstrated that when the intrinsic length is made dependent on damage, the theoretical predictions of strain gradient effects, like thin wire torsion, show strong agreement with experimental data. More recently, [104] expanded on Chen and Wang's [25] lower-order strain gradient plasticity theory, in which the strain gradient affects the immediate tangential stiffness of micro-scale materials, to effectively capture the coupling between size and damage in micro-scale materials. In their model, the damage parameter, which varies with plastic strain, directly impacts both the instantaneous tangential stiffness and the material's intrinsic length scale, enhancing the accuracy of size and damage predictions. While existing models capture some aspects of size dependency and incorporate damage, fully integrating strain gradient plasticity with nonlocal ductile damage remains an underexplored area of research. The challenge of accurately predicting damage at the microscale, especially in metals with both size-dependent phenomena and ductile damage, is still not fully understood.

This thesis aims to develop a constitutive framework and implementation scheme for isotropic ductile damage coupled with a lower-order strain gradient plasticity model. The strain gradient framework is based on the conventional mechanism-based strain gradient (CMSG) theory [27], which itself is grounded in the Taylor dislocation model [105]. CMSG is the lower-order counterpart to the more general higher-order Mechanism-Based Strain Gradient (MSG) theory [18]. Due to its lower-order nature, CMSG offers a robust yet relatively simple implementation. For the isotropic ductile damage model, this work utilizes a non-linear damage law proposed by [91]. An integral-type nonlocal averaging procedure is employed to address localization issues, with the equivalent plastic strain selected as the nonlocal variable. The model's validity is assessed through several benchmark problems, and its performance is evaluated

via a series of mechanical simulations.

The organization of this thesis is as follows: Chapter 2 discusses the formulation and implementation aspects of the CMSG theory in detail. Chapter 3, presents the application of the CMSG theory for a number of different problems. Chapter 4 extends this framework to include a coupled integral-type nonlocal damage law. Chapter 5 presents the results of the CMSG theory coupled with a nonlocal damage law. Finally, Chapter 6 wraps up the thesis with a discussion of key insights and future directions.

CHAPTER 2

REVIEW AND IMPLEMENTATION OF CONVENTIONAL MECHANISM-BASED STRAIN GRADIENT THEORY

In this chapter, formulation, constitutive equations, and finite element implementation of the conventional mechanism-based strain gradient theory are presented. CMSG theory [27] is rooted in Taylor's dislocation model [105] and distinguishes itself from the mechanisms-based strain gradient (MSG) theory [18] by not involving higher-order stresses or any additional boundary conditions. For the implementation, a viscoplastic-like representation of stress is employed, which is rate-insensitive and preserves almost all the characteristics of classical J_2 theory without the need for any additional boundary conditions. In this model, strain gradient is incorporated so that its only effect comes in the calculation of the flow strength of the material. Therefore, it does not require any change in the equilibrium equations, as only the hardening function of the material is modified.

2.1 Formulation of the CMSG Theory

Rooted in Taylor's dislocation model of hardening [105], CMSG theory links the shear stress directly to the dislocation density through the following expression:

$$\tau = \alpha \mu b \sqrt{\rho} \tag{2.1}$$

In this expression, μ refers to the shear modulus, b represents the Burgers vector, and α is an empirical constant, generally ranging from 0.3 to 0.5. The dislocation density ρ is broken down into two parts: ρ_S, representing statistically stored dislocations (SSDs) that result from the random trapping of dislocations [16], and ρ_G, representing geometrically necessary dislocations (GNDs), which are essential for maintaining

deformation compatibility between different regions of the material.

$$\rho = \rho_S + \rho_G \tag{2.2}$$

Effective strain gradient can be related to the GND density, by

$$\rho_G = \bar{r}\frac{\eta^p}{b} \tag{2.3}$$

here, $\bar{r}$, referred to as the Nye factor, generally takes a value of approximately 1.90 for Face-Centered Cubic (FCC) polycrystals [106]. This parameter captures the influence of crystallography on the distribution of GNDs. The shear flow stress τ is subsequently related to the tensile flow stress σ_{flow} by the following expression:

$$\sigma_{flow} = M\tau \tag{2.4}$$

Where M denotes Taylor factor, representing an isotropic approximation of crystal anisotropy at the continuum scale, and for FCC crystals, it typically has a value of $M = 3.06$ [107–109]. Following the substitution of equations (2.1)–(2.3) into (2.4) gives;

$$\sigma_{flow} = M\alpha\mu b\sqrt{\rho_S + \bar{r}\frac{\eta^p}{b}} \tag{2.5}$$

The flow stress is determined by the expression $\sigma_{flow} = \sigma_Y f(\varepsilon^p)$, where σ_Y represents the yield stress, and f is a dimensionless function of plastic strain ε_p, obtained from the uniaxial stress-strain relationship, and is given by:

$$f(\varepsilon^p) = \left(1 + \frac{E\varepsilon^p}{\sigma_Y}\right)^N \tag{2.6}$$

This leads to a power-law hardening behavior, with E representing Young's modulus and N being the plastic hardening exponent, ranging from 0 to 1 $(0 \leqslant N < 1)$.

In order to find the density of statistically stored dislocations ρ_S, a uniaxial tensile loading case is examined. Since this loading yields a uniform strain field, the plastic strain gradient vanishes (i.e., $\eta^p = 0$). Therefore, equation (2.5) can be used to find ρ_S after some manipulations,

$$\rho_S = \left[\frac{\sigma_Y f(\varepsilon^p)}{M\alpha\mu b}\right]^2 \tag{2.7}$$

By substituting the expression for ρ_S back into equation (2.5), the flow stress for non-uniform plastic deformation, which accounts for the influence of GNDs, can be

expressed as:

$$\sigma_{flow} = \sqrt{(\sigma_Y f(\varepsilon^p))^2 + M^2 \bar{r} \alpha^2 b \eta^p} = \sigma_Y \sqrt{f^2(\varepsilon^p) + l\eta^p} \tag{2.8}$$

Where the following renaming of the variable is introduced:

$$l = M^2 \bar{r} \alpha^2 \left(\frac{\mu}{\sigma_Y}\right)^2 b = 18\alpha^2 \left(\frac{\mu}{\sigma_Y}\right)^2 b \tag{2.9}$$

For the given numerical values of $M = 3.06$ and $\bar{r} = 1.90$, it's worth noting that the intrinsic material length l in equation (2.9) naturally combines elasticity μ, yield stress σ_Y, and the atomic structure of materials through the Burgers vector b. In most metals, b is on the order of a nanometer, the ratio of the μ/σ_Y is on the order of hundreds, and α is approximately 0.3. These parameters result in l being on the micron scale, which matches the length scale at which size-dependent effects have been confirmed in experimental studies. For macroscopic plastic deformations, where the intrinsic material length scale l is much smaller than the characteristic length, the strain gradient term $l\eta^p$ in equation (2.8) becomes negligible. This simplifies the flow stress relation to $\sigma_{flow} = \sigma_Y f(\varepsilon^p)$, as seen in conventional plasticity.

2.2 Constitutive Relations

The governing equations of CMSG plasticity are nearly identical to those of conventional plasticity because higher-order terms are not included. The strain rate $\dot{\varepsilon}_{ij}$ can be split into elastic and plastic components, $\dot{\varepsilon}_{ij} = \dot{\varepsilon}^e_{ij} + \dot{\varepsilon}^p_{ij}$. Further, the linear elastic relation can be used to get the elastic strain rate $\dot{\varepsilon}^e_{ij}$ in terms of stress rate $\dot{\sigma}_{ij}$,

$$\dot{\varepsilon}^e_{ij} = \frac{1}{2\mu}\dot{\sigma}^{'}_{ij} + \frac{\dot{\sigma}_{kk}}{9K}\delta_{ij} \tag{2.10}$$

Where $\dot{\sigma}^{'}_{ij} = \dot{\sigma}_{ij} - \frac{1}{3}\dot{\sigma}_{kk}\delta_{ij}$ is the deviatoric part of the stress rate. With K and μ as bulk modulus and shear modulus, respectively. As in conventional J_2 theory, the plastic part of the strain rate $\dot{\varepsilon}^p_{ij}$, is related to the stress deviator $\sigma^{'}_{ij}$ in,

$$\dot{\varepsilon}^p_{ij} = \frac{3\dot{\varepsilon}^p}{2\sigma_e}\sigma^{'}_{ij} \tag{2.11}$$

Using the standard definitions, $\sigma_e = \sqrt{\frac{3}{2}\sigma^{'}_{ij}\sigma^{'}_{ij}}$ for the von Mises equivalent stress, and $\dot{\varepsilon}^p = \sqrt{\frac{2}{3}\dot{\varepsilon}^p_{ij}\dot{\varepsilon}^p_{ij}}$ for the equivalent plastic strain rate, as in conventional rate-independent plasticity theories. As mentioned in the earlier section, non-uniform

deformations which induce plasticity at the micron or in smaller scales, Taylor dislocation model describes the stress as a function dependent of not only the plastic strain ε^p, but also its gradient η^p, meaning $\sigma = \sigma(\varepsilon^p, \eta^p)$. In rate form, this relation can be expressed using the chain rule:

$$\dot{\sigma} = \frac{\partial \sigma}{\partial \varepsilon^p}\dot{\varepsilon^p} + \frac{\partial \sigma}{\partial \eta^p}\dot{\eta^p} \tag{2.12}$$

Afterward, equation (2.12) can be substituted into equation (2.11) for a plastic strain rate $\dot{\varepsilon}^p_{ij}$ proportional to the deviatoric stress $\sigma^{'}_{ij}$ prevents the formulation of a fully self-contained constitutive model due to the inclusion of the term $\dot{\eta}^p$. In fact, the main reason behind the necessity for higher order stress terms in the classical MSG (developed by [18, 19]) theory is this. To address this issue, without resorting to a higher-order constitutive relation, [27] implemented a viscoplastic-like formulation that expresses $\dot{\varepsilon}^p$ in terms of the von Mises effective stress σ_e instead of its rate $\dot{\sigma}_e$ (some examples of this approach can be seen [110–112]):

$$\dot{\varepsilon^p} = \dot{\varepsilon_0}\left[\frac{\sigma_e}{\sigma_{flow}}\right]^m \tag{2.13}$$

Where ε_0 is termed as the reference strain rate, with the rate sensitivity exponent given as m, having typically larger numerical values (i.e., $m \geqslant 20$), and σ_{flow} represents the flow stress defined in equation (2.8). For the limit where $m = \infty$, equation (2.13) is equalivalent to $\sigma = \sigma_Y f(\varepsilon_p)$ for a uniaxial tension test. A single-element uniaxial test is conducted to see the effect of rate sensitivity exponent m. From Figure 2.1, as the values of m get larger, the effect becomes more negligible.

A viscoplastic-like approach, as seen in [113], can be employed in order to reduce the impact of strain rate and time dependence. In this approach, the reference strain rate $\dot{\varepsilon}_0$ is replaced by the von Mises effective strain rate $\dot{\varepsilon}$. This modification is purely for mathematical convenience, and [27] has shown that it has a negligible effect when m is large (specifically, for $m \geqslant 20$). Throughout the analyses done in this thesis, unless stated otherwise, this parameter has been taken as $m = 20$. With this slight modification, equation (2.13) becomes,

$$\dot{\varepsilon^p} = \dot{\varepsilon}\left[\frac{\sigma_e}{\sigma_{flow}}\right]^m \tag{2.14}$$

With $\dot{\varepsilon} = \sqrt{\frac{2}{3}\dot{\varepsilon}^{'}_{ij}\dot{\varepsilon}^{'}_{ij}}$, and $\dot{\varepsilon}^{'}_{ij} = \dot{\varepsilon}_{ij} - \frac{1}{3}\dot{\varepsilon}_{kk}\delta_{ij}$ as the deviatoric strain rate. The volumetric and deviatoric parts of strain rates can be readily obtained from equations (2.10)

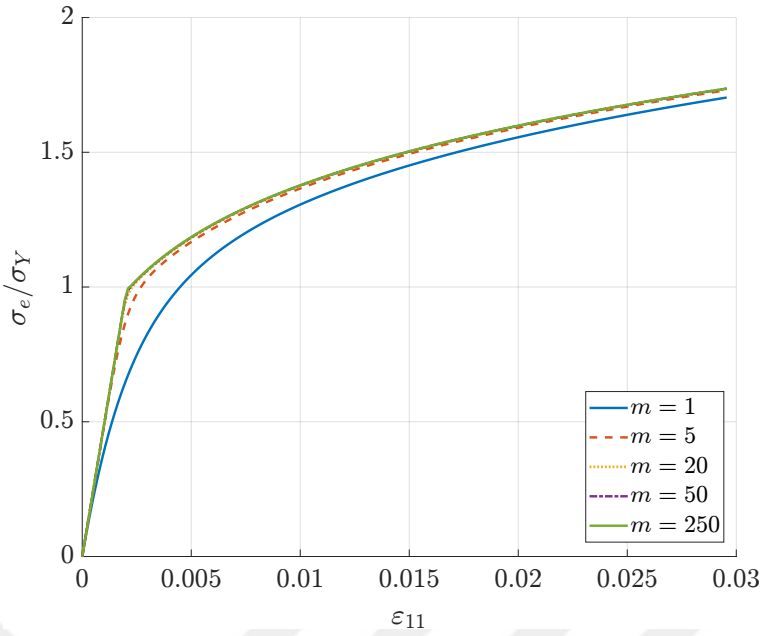

Figure 2.1: A uniaxial stress-strain test is conducted on a single element for values of $m = 1, 5, 20, 50$, and 250. Here, σ_Y represents the initial yield stress, and σ_e denotes the effective stress, with a power-law hardening exponent of $N = 0.2$. The yield stress to Young's modulus ratio is given by $\sigma_Y/E = 0.002$, and the Poisson's ratio is $\nu = 0.3$.

and (2.11) as

$$\dot{\varepsilon}_{kk} = \frac{\dot{\sigma}_{kk}}{3K} \tag{2.15}$$

$$\dot{\varepsilon}'_{ij} = \frac{\sigma'_{ij}}{2\mu} + \frac{3\dot{\varepsilon}^p}{2\sigma_e}\sigma'_{ij} \tag{2.16}$$

Substituting the σ_{flow} given in equation (2.8) into the equivalent plastic strain rate $\dot{\varepsilon}$ in equation (2.14), yields an equation which accounts for strain gradient effects based on Taylor dislocation model without dealing with higher order terms:

$$\dot{\varepsilon}^p = \dot{\varepsilon}\left[\frac{\sigma_e}{\sigma_{flow}}\right]^m = \dot{\varepsilon}\left[\frac{\sigma_e}{\sigma_Y\sqrt{f^2(\varepsilon^p) + l\eta^p}}\right]^m \tag{2.17}$$

Further, the strain rate can be obtained by substitution of equation (2.17) into equations (2.15) and (2.16) after some manipulations:

$$\dot{\varepsilon}_{ij} = \frac{\dot{\sigma}_{kk}}{9K}\delta_{ij} + \frac{\dot{\sigma}'_{ij}}{2\mu} + \frac{3\dot{\varepsilon}}{2\sigma_e}\left(\frac{\sigma_e}{\sigma_Y\sqrt{f^2(\varepsilon^p) + l\eta^p}}\right)^m \sigma'_{ij} \tag{2.18}$$

Stress rate can also be obtained by inverting the above relation as:

$$\dot{\sigma}_{ij} = K\dot{\varepsilon}_{kk}\delta_{ij} + 2\mu\left[\dot{\varepsilon}'_{ij} - \frac{3\dot{\varepsilon}}{2\sigma_e}\left(\frac{\sigma_e}{\sigma_Y\sqrt{f^2(\varepsilon^p) + l\eta^p}}\right)^m \sigma'_{ij}\right] \tag{2.19}$$

It can be noted here that, for an increase in effective plastic strain gradient η^p, the plastic strain rate decreases which corresponds well with the experimental observations. Because the effective plastic strain gradient diminishes the plastic incremental moduli, it aligns with the lower-order framework of strain gradient plasticity theories [30]. In, [114] an alternative approach following solely viscoplastic approach can be found.

2.2.1 Definition of effective plastic strain gradient

According to equation (2.8), the flow stress σ_{flow} is determined by the plastic strain ε^p, which is inherently non-decreasing, and effective plastic strain gradient η^p. As per the definition of effective plastic strain gradient η^p, this thesis adopts the definition proposed by [18], which utilizes geometrically necessary dislocations to compute η^p. In its most general form, this expression reads:

$$\eta^p = \sqrt{c_1\eta^p_{iik}\eta^p_{jjk} + c_2\eta^p_{ijk}\eta^p_{ijk} + c_3\eta^p_{ijk}\eta^p_{kji}} \tag{2.20}$$

with,

$$\eta^p_{ijk} = \varepsilon^p_{ik,j} + \varepsilon^p_{jk,i} - \varepsilon^p_{ij,k} \tag{2.21}$$

The parameters c_1, c_2, and c_3 denote the three quadratic invariants associated with the third-order tensor η^p_{ijk}. These quadratic invariants have been numerically evaluated using a series of dislocation models, which include plane strain bending, pure torsion, and axisymmetric void growth. The objective is to identify the values of these quadratic invariants that optimize the configuration of geometrically necessary dislocations, thereby minimizing their density under given specific deformation conditions. According to the findings of [18, 115] the most suitable invariant values that favor minimum geometrically necessary dislocation densities are $c_1 = c_3 = 0$, and $c_2 = 1/4$. This leads to the definition of effective plastic strain gradient η^p as:

$$\eta^p = \sqrt{\frac{1}{4}\eta^p_{ijk}\eta^p_{ijk}} \tag{2.22}$$

Alternatively, in an incremental form, equation (2.22), can be expressed as (under rate-proportional loading);

$$\Delta\eta^p = \sqrt{\frac{1}{4}\Delta\eta^p_{ijk}\Delta\eta^p_{ijk}} \tag{2.23}$$

2.3 Derivation of the Tangent Stiffness Matrix

Unlike the higher-order MSG theory [18, 19], CMSG is a lower-order theory, which means it does not include higher-order stresses in its constitutive relations. As a result, the governing equations are similar to those in classical plasticity, allowing for more straightforward implementation of the constitutive relations, as shown in equations (2.18) and (2.19). These implementations are performed in the commercial finite element software ABAQUS via a user material subroutine. In this section, the consistent tangent modulus, essential for the ABAQUS subroutine, is derived. From a classical perspective, the strain tensor can be expressed as a sum of its elastic and plastic components:

$$\varepsilon_{ij} = \varepsilon^e_{ij} + \varepsilon^p_{ij} \tag{2.24}$$

With ε^e_{ij}, and ε^p_{ij} representing the elastic and plastic parts, respectively. The deviatoric part of the strain tensor can be given as;

$$\varepsilon'_{ij} = \varepsilon_{ij} - \frac{1}{3}\varepsilon_{kk}\delta_{ij} \tag{2.25}$$

Alternatively in its decomposed form with elastic and plastic parts:

$$\varepsilon'^e_{ij} = \varepsilon^e_{ij} - \frac{1}{3}\varepsilon_{kk}\delta_{ij} \tag{2.26}$$

$$\varepsilon'^p_{ij} = \varepsilon^p_{ij} \tag{2.27}$$

With the deviatoric part of the elastic strain tensor denoted as ε'^e_{ij} in relation to the deviatoric stress tensor σ'_{ij}, by Hooke's law. Specifically this expression reads:

$$\sigma'_{ij} = 2\mu\varepsilon'^e_{ij} = \sigma_{ij} - \frac{1}{3}\sigma_{kk}\delta_{ij} \tag{2.28}$$

Where the plastic strain increment $\Delta\varepsilon^p_{ij}$ is related to the deviatoric part of the stress tensor σ'_{ij}, similar to the classical J_2-flow theory. The equation (2.11), given in rate

form, can be written in incremental terms with values evaluated at the end of the current timestep as follows:

$$\Delta\varepsilon_{ij}^{p} = \frac{3\Delta\varepsilon^{p}}{2\sigma_e}\sigma'_{ij} = \frac{3\Delta\varepsilon(\sigma_e/\sigma_{flow})^{m}}{2\sigma_e}\sigma'_{ij} \tag{2.29}$$

Where the definition of $\dot{\varepsilon}^{p}$ given in equation (2.14) in incremental form is substituted and $\Delta\varepsilon = \sqrt{\frac{2}{3}\varepsilon_{ij}\varepsilon_{ij}}$ is denoted as the incremental effective strain. By substituting equation (2.29) into (2.28) and considering the deviatoric elastic strain tensor $\varepsilon_{ij}^{\prime e}$, at the end of an increment the deviatoric stress can be obtained as:

$$\sigma'_{ij} = 2\mu\left(\varepsilon_{ij}^{\prime e}|_t + \Delta\varepsilon'_{ij} - \Delta\varepsilon_{ij}^{p}\right) \tag{2.30}$$

Substitution of equation (2.29) into (2.30) yields:

$$\sigma'_{ij} = 2\mu\left(\varepsilon_{ij}^{\prime e}|_t + \Delta\varepsilon'_{ij} - \frac{3\Delta\varepsilon^{p}}{2\sigma_e}\sigma'_{ij}\right) \tag{2.31}$$

Where for simplicity, following renaming is defined $\hat{e}_{ij} = \varepsilon_{ij}^{\prime e}|_t + \Delta\varepsilon'_{ij}$. Where, $\varepsilon_{ij}^{\prime e}|_t$, representing the deviatoric part of the elastic strain tensor evaluated at the beginning of the increment and, $\Delta\varepsilon'_{ij}$ is given as the total deviatoric strain from the current increment. After rearranging, equation (2.31) reads:

$$\left(1 + \frac{3\mu}{\sigma_e}\Delta\varepsilon^{p}\right)\sigma'_{ij} = 2\mu\hat{e}_{ij} \tag{2.32}$$

Taking the inner product of equation (2.32) with itself yields:

$$\left(1 + \frac{3\mu}{\sigma_e}\Delta\varepsilon^{p}\right)^{2}\left(\sigma'_{ij}\sigma'_{ij}\right) = (2\mu)^{2}\left(\hat{e}_{ij}\hat{e}_{ij}\right) \tag{2.33}$$

Defining $\tilde{e} = \sqrt{\frac{2}{3}\hat{e}_{ij}\hat{e}_{ij}}$, and using the identity $\sigma_e = \sqrt{\frac{3}{2}\sigma'_{ij}\sigma'_{ij}}$ the equation (2.33) can be written concisely:

$$\sigma_e + 3\mu\Delta\varepsilon^{p} = 3\mu\tilde{e} \tag{2.34}$$

Re-arranging equation (2.34) and substituting equation (2.29) results in,

$$\sigma_e - 3\mu\left(\tilde{e} - \Delta\varepsilon\left(\frac{\sigma_e}{\sigma_{flow}}\right)^{m}\right) = 0 \tag{2.35}$$

The Newton's method can be used to solve for σ_e:

$$\sigma_e = \sigma_e + \frac{3\mu\left(\tilde{e} - \Delta\varepsilon\left(\frac{\sigma_e}{\sigma_{flow}}\right)^{m}\right) - \sigma_e}{1 + 3\mu h} \tag{2.36}$$

With h given as:

$$h = m\Delta\varepsilon \left(\frac{\sigma_e}{\sigma_{flow}} \right)^{m-1} \frac{1}{\sigma_{flow}} \tag{2.37}$$

Once equation (2.36) converges, the effective plastic strain increment can be found from:

$$\Delta\varepsilon^p = \tilde{e} - \frac{\sigma_e}{3\mu} \tag{2.38}$$

Thus, $\sigma_{ij}^{'}$ can be determined using equation (2.32), while $\Delta\varepsilon_{ij}^p$ is obtained from the incremental form of equation (2.11). The consistent material Jacobian $\partial\Delta\sigma_{ij}/\partial\Delta\varepsilon_{ij}$ is subsequently determined by differentiating equation (2.32) with respect to all pertinent quantities at the conclusion of the increment.

$$\left(1 + \frac{3\mu}{\sigma_e}\Delta\varepsilon^p\right)\partial\sigma'_{ij} + \sigma'_{ij}\frac{3\mu}{\sigma_e}\left(\partial\Delta\varepsilon^p - \frac{\Delta\varepsilon^p}{\sigma_e}\partial\sigma_e\right) = 2\mu\partial\hat{e}_{ij} \tag{2.39}$$

Similarly, variation of equation (2.34) gives;

$$\partial\sigma_e + 3\mu\partial\Delta\varepsilon^p = 3\mu\partial\tilde{e} \tag{2.40}$$

Substituting back equation (2.38), and rearranging yields,

$$\partial\sigma_e = \frac{3\mu}{1 + 3\mu h}\partial\tilde{e} \tag{2.41}$$

Taking into account the definition of $\tilde{e}$ results in,

$$\partial\sigma_e = \frac{2}{3\tilde{e}}\frac{3\mu}{1 + 3\mu h}\hat{e}_{ij}\partial\hat{e}_{ij} \tag{2.42}$$

Substituting back into equation (2.39) and after rearranging,

$$\partial\sigma'_{ij} = \left(\frac{2\sigma_e}{3\tilde{e}}I^{(4)}_{ijkl} - \frac{1}{\sigma_e\tilde{e}}\left(h - \frac{\Delta\varepsilon^p}{\sigma_e}\right)\frac{3\mu}{1 + 3\mu h}\sigma'_{ij}\sigma'_{kl}\right)\partial\hat{e}_{kl} \tag{2.43}$$

In this case, the fourth-order unit tensor is represented by $I^{(4)}_{ijkl}$. Following this, the material tangent can be defined by examining the relationship between the stress and strain tensors, including their deviatoric components, as follows:

$$\partial\sigma_{ij} = \left(\frac{2\sigma_e}{3\hat{\varepsilon}}I^{(4)}_{ijkl} + \left(K - \frac{2\sigma_e}{9\tilde{e}}\right)I_{ij}I_{kl} - \frac{1}{\sigma_e\tilde{e}}\left(h - \frac{\Delta\varepsilon^p}{\sigma_e}\right)\frac{3\mu}{1 + 3\mu h}\sigma'_{ij}\sigma'_{kl}\right)\partial\varepsilon_{kl} \tag{2.44}$$

2.4 Finite Element Implementation of CMSG Theory

This section presents two distinct approaches for calculating the strain gradient tensor, each offering a different method for evaluating the gradient field based on plastic strain values. The first approach involves an interpolation procedure conducted within each element, where the plastic strains computed at the integration points are used to determine the strain gradient. This method relies on the derivatives of the shape functions within the element to calculate the gradients, effectively treating the element in isolation. Neighboring elements do not contribute to the calculation, and thus the strain gradients are entirely localized within the element. While this method offers simplicity and ease of implementation, its limitation lies in its inability to account for interactions between neighboring elements, which can be critical for capturing strain gradient effects over larger regions.

The second approach is more comprehensive, involving the extrapolation of plastic strains from the integration points to the nodes. Since nodes are shared by multiple elements, this method introduces an averaging procedure to regularize the plastic strain values at each node. The plastic strains from adjacent elements are averaged at these nodal points to produce a smoother, more globally consistent strain distribution. Once the averaged nodal values are obtained, they are used to compute the strain gradients at the nodes, which are subsequently projected back onto the integration points to achieve element-wise strain gradients. This method allows for a more accurate representation of strain gradients in areas where neighboring element interactions are significant, making it particularly useful for problems where gradient continuity across element boundaries is essential.

Both approaches have been successfully implemented in both two-dimensional and three-dimensional finite element settings. In the two-dimensional implementation, 4-noded quadrilateral plane strain elements with full integration (CPE4) are used. Conversely, the three-dimensional implementation employs 8-node continuum elements with full integration (C3D8).

2.4.1 Interpolation Method

In addition to the constitutive relations, evaluating the plastic strain gradient within the UMAT is necessary, as the equilibrium equations, boundary conditions, and kinematic relationships between the strain and displacement fields are the same as in classical plasticity. In three dimensional setting, the plastic strains within the element can be obtained as:

$$\Delta\varepsilon_{ij}^{p} = \sum_{k=1}^{8} N_k^g(x, y, z) \left(\Delta\varepsilon_{ij}^{p}\right)_k \tag{2.45}$$

In this context, N_k^g denotes the interpolation function in global coordinates, while $\left(\Delta\varepsilon_{ij}^{p}\right)_k$ represents the incremental values of plastic strain at the integration (Gauss) points. Given that C3D8 elements are used, which have eight integration points, the summation in equation (2.45) runs from one to eight. The global interpolation function is obtained through the classical isoparametric coordinate transformation as follows:

$$x = \sum_{k=1}^{8} N_k(\xi, \eta, \zeta) x_k \tag{2.46}$$

$$y = \sum_{k=1}^{8} N_k(\xi, \eta, \zeta) y_k \tag{2.47}$$

$$z = \sum_{k=1}^{8} N_k(\xi, \eta, \zeta) z_k \tag{2.48}$$

Here ξ, η, and ζ represent the local coordinate system. The numbering convention for integration points and the nodes can be seen in Figure 2.2. For simplicity, the interpolation function in local coordinates is formulated similarly to the shape functions, resulting in equation (2.45) becoming:

$$\Delta\varepsilon_{ij}^{p} = \sum_{k=1}^{8} N_k(\xi, \eta, \zeta) \left(\Delta\varepsilon_{ij}^{p}\right)_k \tag{2.49}$$

With three-dimensional linear shape functions adopted as:

$$N_i = \frac{1}{8}(1 + \xi\xi_i)(1 + \eta\eta_i)(1 + \zeta\zeta_i) \tag{2.50}$$

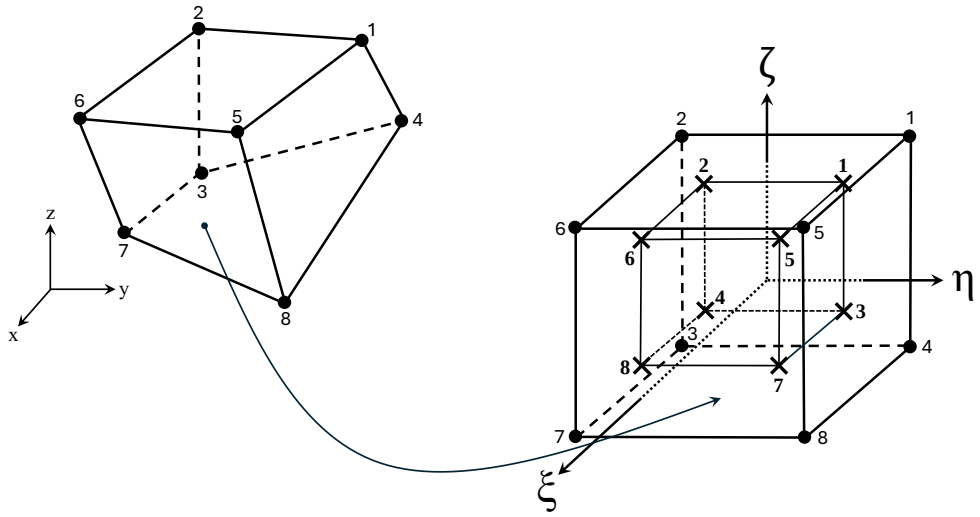

Figure 2.2: Numbering schemes used in 3D hexahedral elements (C3D8) in both global and isoparametric (natural) spaces.

Differenciating the shape functions therefore yields the following:

$$\frac{\partial N_i}{\partial \xi} = \frac{1}{8}\xi_i(1+\eta\eta_i)(1+\zeta\zeta_i) \tag{2.51}$$

$$\frac{\partial N_i}{\partial \eta} = \frac{1}{8}\eta_i(1+\xi\xi_i)(1+\zeta\zeta_i) \tag{2.52}$$

$$\frac{\partial N_i}{\partial \zeta} = \frac{1}{8}\zeta_i(1+\xi\xi_i)(1+\eta\eta_i) \tag{2.53}$$

To convert the shape function derivatives given in equations (2.51), (2.52), and (2.53) the chain rule can be applied as follows:

$$\begin{bmatrix} \frac{\partial N_k}{\partial x} \\ \frac{\partial N_k}{\partial y} \\ \frac{\partial N_k}{\partial z} \end{bmatrix} = J^{-1} \begin{bmatrix} \frac{\partial N_k}{\partial \xi} \\ \frac{\partial N_k}{\partial \eta} \\ \frac{\partial N_k}{\partial \zeta} \end{bmatrix} \tag{2.54}$$

Where, J is the Jacobian matrix given as:

$$J = \begin{bmatrix} \frac{\partial x}{\partial \xi} & \frac{\partial y}{\partial \xi} & \frac{\partial z}{\partial \xi} \\ \frac{\partial x}{\partial \eta} & \frac{\partial y}{\partial \eta} & \frac{\partial z}{\partial \eta} \\ \frac{\partial x}{\partial \zeta} & \frac{\partial y}{\partial \zeta} & \frac{\partial z}{\partial \zeta} \end{bmatrix} = \begin{bmatrix} \sum_{k=1}^{8} \frac{\partial N_k}{\partial \xi} x_k & \sum_{k=1}^{8} \frac{\partial N_k}{\partial \xi} y_k & \sum_{k=1}^{8} \frac{\partial N_k}{\partial \xi} z_k \\ \sum_{k=1}^{8} \frac{\partial N_k}{\partial \eta} x_k & \sum_{k=1}^{8} \frac{\partial N_k}{\partial \eta} y_k & \sum_{k=1}^{8} \frac{\partial N_k}{\partial \eta} z_k \\ \sum_{k=1}^{8} \frac{\partial N_k}{\partial \zeta} x_k & \sum_{k=1}^{8} \frac{\partial N_k}{\partial \zeta} y_k & \sum_{k=1}^{8} \frac{\partial N_k}{\partial \zeta} z_k \end{bmatrix} \tag{2.55}$$

Jacobian matrix describes the derivatives of the global coordinates in relation to the natural coordinate system. With the plastic strain gradient definition from equation

(2.21), components of effective plastic strain gradient increment $\Delta\eta^p$ within the element can be computed as:

$$\Delta\eta^p_{ijk} = \sum_{m=1}^{8} \frac{\partial N_m}{\partial x_j}(\Delta\varepsilon^p_{ik})_m + \sum_{m=1}^{8} \frac{\partial N_m}{\partial x_i}(\Delta\varepsilon^p_{jk})_m + \sum_{m=1}^{8} \frac{\partial N_m}{\partial x_k}(\Delta\varepsilon^p_{ij})_m \tag{2.56}$$

Where x_i (for $i = 1, 2, 3$) denote x, y, and z coordinates respectively.

Furthermore, for the two-dimensional implementation, slight modifications are required. Since 4 noded quadrilateral plane strain elements (CPE4) given in Figure (2.3) are used. The shape functions are modified as:

$$N_i = \frac{1}{4}(1 + \xi\xi_i)(1 + \eta\eta_i) \tag{2.57}$$

Further, the shape function derivatives given in equations (2.51)-(2.53) become:

$$\frac{\partial N_i}{\partial \xi} = \frac{1}{4}\xi_i(1 + \eta\eta_i) \tag{2.58}$$

$$\frac{\partial N_i}{\partial \eta} = \frac{1}{4}\eta_i(1 + \xi\xi_i) \tag{2.59}$$

Therefore changing the Jacobian given in equation (2.55) into:

$$J = \begin{bmatrix} \frac{\partial x}{\partial \xi} & \frac{\partial y}{\partial \xi} \\ \frac{\partial x}{\partial \eta} & \frac{\partial y}{\partial \eta} \end{bmatrix} = \begin{bmatrix} \sum_{k=1}^{4} \frac{\partial N_k}{\partial \xi} x_k & \sum_{k=1}^{4} \frac{\partial N_k}{\partial \xi} y_k \\ \sum_{k=1}^{4} \frac{\partial N_k}{\partial \eta} x_k & \sum_{k=1}^{4} \frac{\partial N_k}{\partial \eta} y_k \end{bmatrix} \tag{2.60}$$

For four integration points, the summation in the equation (2.60) runs from one to four. Finally the equation (2.21) for two-dimensions becomes:

$$\Delta\eta^p_{ijk} = \sum_{m=1}^{4} \frac{\partial N_m}{\partial x_j}(\Delta\varepsilon^p_{ik})_m + \sum_{m=1}^{4} \frac{\partial N_m}{\partial x_i}(\Delta\varepsilon^p_{jk})_m + \sum_{m=1}^{4} \frac{\partial N_m}{\partial x_k}(\Delta\varepsilon^p_{ij})_m \tag{2.61}$$

Where, x_i (for $i = 1, 2$) denote the x and y coordinates, respectively. Since the derivatives of the shape functions with respect to the z-axis, $\partial N/\partial z$, are zero, only fourteen out of the twenty-seven components in the plastic strain gradient tensor η^p_{ijk} are non-zero. Under the plane strain assumption, the incompressibility condition can be used to determine the out-of-plane plastic strain increment, $\Delta\varepsilon^p_{33}$, as follows:

$$\Delta\varepsilon^p_{33} = -(\Delta\varepsilon^p_{11} + \Delta\varepsilon^p_{22}) \tag{2.62}$$

In this approach, since the values at the integration points are interpolated, the effective plastic strain gradient remains confined within the element. Since for this

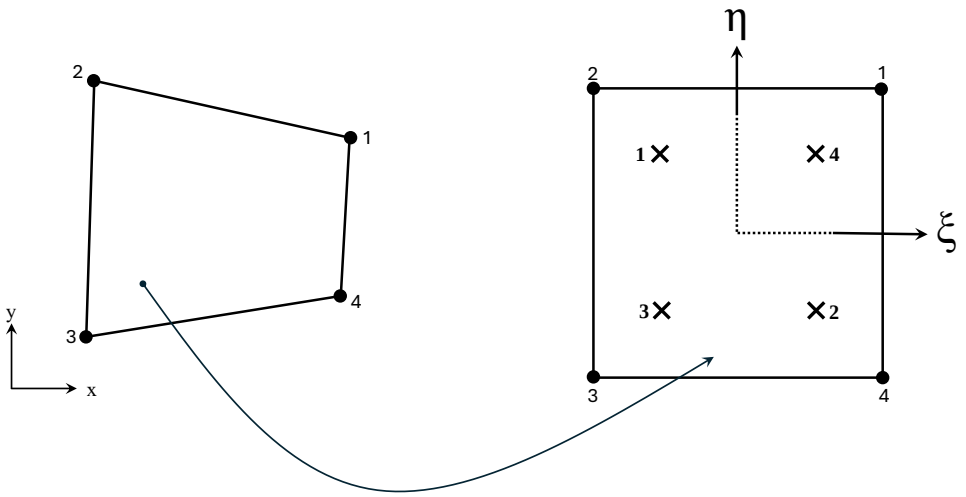

Figure 2.3: Numbering schemes used in 2D quadrilateral plane strain elements (CPE4) in both global and isoparametric (natural) spaces.

method computations are performed on a single element by element basis, it offers more robustness. In the FE implementation of the interpolation method, the plastic strain gradient increment, $\Delta\eta^p$, is obtained using a staggered scheme. This requires the incremental values of plastic strains and the global coordinates of the integration points. To facilitate this, the plastic strain increments, $\Delta\varepsilon_{ij}^p$, along with the integration point coordinates at the end of each increment, are stored in a global FORTRAN module. This setup allows for access to these values when calculating the plastic strain gradient in the current increment.

At each increment, a loop iterates through all the integration points, utilizing the previously stored values to compute the plastic strain gradient increment. Initially, the shape function derivatives are evaluated. For 3D formulations, equations (2.51)-(2.53) are used, while for 2D formulations, equations (2.58)-(2.59) are employed. These derivatives are calculated and evaluated at the nodal point coordinates in the isoparametric space, enabling interpolation within the element.

Subsequently, the element Jacobian is constructed using the previously stored integration point coordinates. This matrix is then inverted and multiplied by the shape function derivatives, as shown in equation (2.54). Therefore, the derivatives of the

shape functions with respect to the global coordinate system can be obtained. Afterward, the previously stored plastic strain increments are multiplied by these derivatives according to equation (2.56) to yield the plastic strain gradient increment.

Upon completing these steps for all integration points, the plastic strain gradient increment values for all integration points are determined. These values are then used in equation (2.8) to calculate the flow stress in the current increment.

2.4.2 Extrapolation and Nodal Averaging method

In the previous section, it was established that the effective plastic strain gradient increment, $\Delta\eta^p$, and the total effective plastic strain gradient, η^p, are variables calculated on an element-by-element basis. This section explores the potential influences from neighboring elements. This is achieved by first extrapolating the incremental plastic strain values, $\Delta\varepsilon^p_{ij}$, determined at Gaussian integration points to the nodes. In a three-dimensional context, the plastic strain increments at the nodes are obtained by extrapolating these values. This process involves inverting the shape function matrix, which is used to interpolate nodal values to integration points:

$$\Delta\varepsilon^p_{ij,IPT} = \sum_{k=1}^{8} N_k(\xi,\eta,\zeta)\left(\Delta\varepsilon^p_{ij,N}\right)_k \tag{2.63}$$

$$\Delta\varepsilon^p_{ij,N} = \sum_{k=1}^{8} N_k^{-1}(\xi,\eta,\zeta)\left(\Delta\varepsilon^p_{ij,IPT}\right)_k \tag{2.64}$$

where $\Delta\varepsilon^p_{ij,N}$ denotes the incremental nodal values of the plastic strains, and $\Delta\varepsilon^p_{ij,IPT}$ are the integration point values. Again, linear shape functions given in equation (2.50) are employed. Hence, plastic strain values at the nodes can be obtained. However, because each node is tied to several elements, different plastic strain values will be assigned to the same node for each element to which it is attached. To overcome this and ensure the continuity of an otherwise discontinuous field, a nodal averaging scheme is employed. Figure 2.4 depicts the basic concept of this technique for a one-dimensional case. After nodal averaging is performed, the shape function derivatives are evaluated at their corresponding Gauss integration points. Next, the element Jacobian using the nodal coordinates is constructed. Therefore, the spatial derivative of

the plastic strains can be written as:

$$\nabla \varepsilon^p_{ij,IPT} = \frac{\partial \varepsilon^p_{ij,IPT}}{\partial \boldsymbol{\psi}} \frac{\partial \boldsymbol{\psi}}{\partial \boldsymbol{x}} = \frac{\left(\sum_{k=1}^{8} N_k \left(\varepsilon^p_{ij,N} \right)_k \right)}{\partial \boldsymbol{\psi}} \frac{\partial \boldsymbol{\psi}}{\partial \boldsymbol{x}} \tag{2.65}$$

In a concise form, equation (2.65) can be written as;

$$\nabla \varepsilon^p_{ij,IPT} = \nabla_{\boldsymbol{\psi}} \left(\sum_{k=1}^{8} N_k \right) \left(\varepsilon^p_{ij,N} \right)_k J^{-1} \tag{2.66}$$

Where, $\nabla_{\boldsymbol{\psi}} \left(\sum_{k=1}^{8} N_k \right)$ denotes the gradient of shape functions with respect to isoparametric coordinates. Therefore, equation (2.21) becomes:

$$\eta^p_{ijk} = \sum_{m=1}^{8} \frac{\partial N_m}{\partial \psi_j} \varepsilon^p_{ik,N} J^{-1} + \sum_{m=1}^{8} \frac{\partial N_m}{\partial \psi_i} \varepsilon^p_{jk,N} J^{-1} - \sum_{m=1}^{8} \frac{\partial N_m}{\partial \psi_k} \varepsilon^p_{ij,N} J^{-1} \tag{2.67}$$

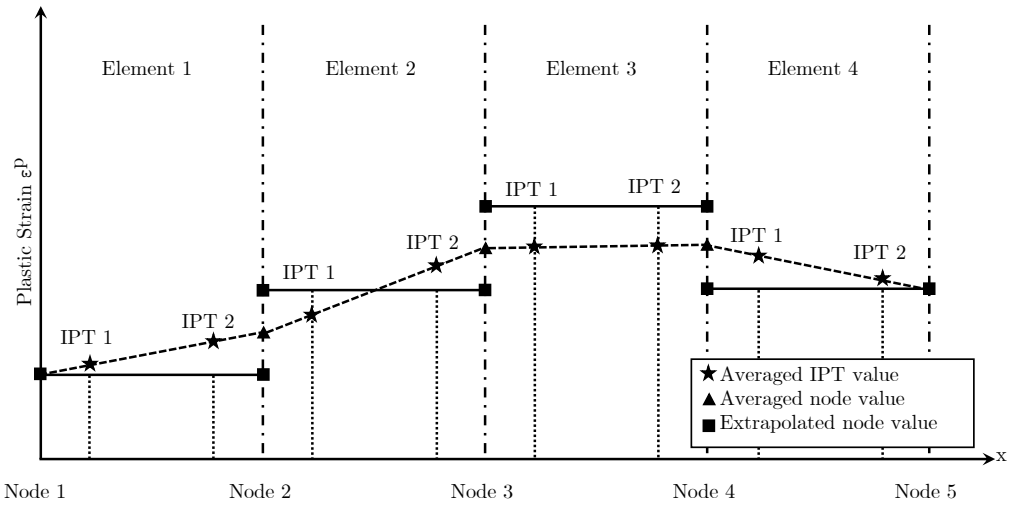

Figure 2.4: Schematic of the nodal averaging method shown in 1D with 5 elements.

Where, ψ_i (for $i = 1, 2, 3$) denote ξ, η, and ζ coordinates in isoparametric space respectively.

Similar to the previously discussed implementation, local values of the plastic strain increments are obtained at the integration points. At the end of each increment, these plastic strain increments are multiplied by the inverse of the shape functions to determine the plastic strain increments at the nodes. These nodal values, along with the nodal coordinates, are then stored in a global FORTRAN array to calculate the plastic

strain gradient. ABAQUS's URDFIL utility subroutine is used to store the nodal coordinates. For nodal averaging, a Matlab preprocessor script reads the input file and records the element-node connectivity in an array, which is then read by the UMAT subroutine using UEXTERNALDB.

The UEXTERNALDB subroutine, invoked at the end of each increment, handles the nodal averaging process. It uses the element connectivity array to loop over all elements, identifying common nodes and averaging the values stored at these nodes. Once the nodal averaging is completed, these averaged values are returned to the UMAT for use in the next increment, enabling a staggered plastic strain gradient calculation. It should be noted here that unlike the implementation of the interpolation method explained in the previous section, the shape function derivatives are evaluated at the Gauss integration point coordinates at the parametric space, and the element Jacobian matrix is constructed using the integration point coordinates. Since, in the previous implementation, only single elements are considered for the calculation of the strain gradient, it offers a good approximation for the calculation of the strain gradients. However, this method ensures continuity and consistency across elements.

CHAPTER 3

APPLICATIONS OF CMSG THEORY

This chapter presents application of CMSG plasticity theory to various problems in order to investigate the performance of two different methods for calculating strain gradients: the interpolation method and the extrapolation method. The aim is to examine the similarities and differences between these methods and evaluate their predictive capabilities in modeling size-dependent plastic deformation in micro and nanostructured materials. The interpolation method calculates strain gradients at the element level, disregarding the effects of neighboring elements, while the extrapolation method employs a nodal averaging scheme to incorporate neighboring element effects.

The CMSG theory is applied to three distinct problems. The first is a bimaterial system, where the focus is on analyzing the interface between two dissimilar materials, presenting a challenging test for capturing interface effects and material mismatch. The second problem involves wire torsion, a canonical example in strain gradient plasticity where size effects significantly influence the material's torsional response. The third problem explores particle-reinforced composites, where the non-uniform deformation due to the inclusion of particles is induced, providing a complex setting for evaluating the accuracy of the strain gradient calculations.

3.1 Analysis of a Bimaterial Interface

The first problem involves a bimaterial system, where two dissimilar materials are joined at an interface. This problem serves as a key test for CMSG theory, particularly in capturing the complex mechanical behavior at the interface between materials with

differing properties. Both the interpolation and extrapolation methods for calculating strain gradients are applied to this problem, allowing for a detailed comparison of how each method captures the size-dependent plasticity and strain gradient effects at the interface. The primary goal here is to evaluate how these two methods handle the stress concentrations and gradient effects that arise due to the material mismatch at the interface. A thin bimaterial plate is tested to create strain gradients at the interface between the two materials. The analysis is conducted with five different mesh sizes, each progressively refined until convergence is achieved. The material properties are listed below. Figure 3.1 illustrates the geometry, material placement, and boundary conditions, showing a rectangular plate with a side length of $L_0 = 3\,\mathrm{mm}$ and a height of $h = 1.5\,\mathrm{mm}$. For the boundary conditions, a horizontal displacement of $\delta = 0.2\,\mathrm{mm}$ is applied at the far end with the near side of the model fixed to prevent rigid body motion.

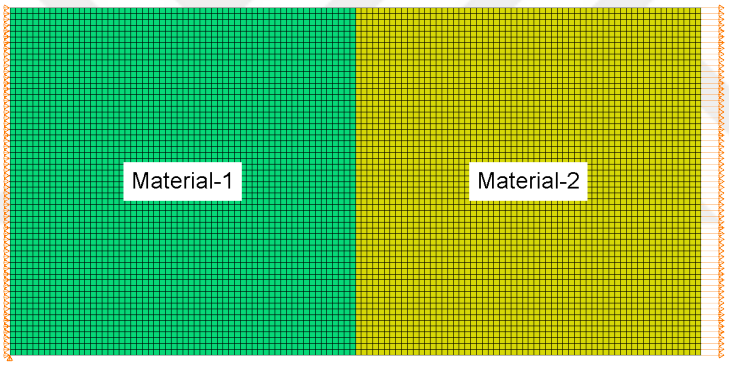

Figure 3.1: Discretization and material placement for the bimaterial interface analaysis (mesh taken from M_2).

To ensure accurate results and mesh convergence, five different mesh configurations were employed. All elements used in these meshes are two dimensional square, quadrilateral, 4-noded plane strain elements (CPE4) in two dimensions. The first mesh utilized a coarser element size of $\Delta x_1 = 50\,\mu\mathrm{m}$ with a total of $M_1 = 1800$ elements. The second mesh refined the element size to $\Delta x_2 = 25\,\mu\mathrm{m}$, increasing the total number of elements to $M_2 = 7200$. The third mesh featured a medium-fine configuration with an element size of $\Delta x_3 = 12.5\,\mu\mathrm{m}$ and $M_3 = 28800$ elements. This was followed by a fourth mesh with a finer element size of $\Delta x_4 = 16\,\mu\mathrm{m}$ and

$M_4 = 70688$ elements. Finally, the fifth and finest mesh had an element size of $\Delta x_5 = 6.25\,\mu\text{m}$ and a total of $M_5 = 115200$ elements. With each successive mesh, the element size was reduced, improving the resolution of the strain gradient calculation and ensuring convergence of the numerical solution. Figure 3.3 presents the

Table 3.1: Material properties for the bimaterial interface analysis.

Name	E [GPa]	ν	σ_Y [MPa]	l [μm]	N
Mat-1	100	0.33	200	5	0.2
Mat-2	80	0.3	300	10	0.136

strain gradient distributions for the four finest mesh sizes. The extrapolation and nodal averaging method effectively captures the strain gradients that develop along the interface boundary, visible in the figure as a strip of high strain gradients. In contrast, the interpolation method shows a sudden drop in the strain gradient distribution at the interface, as it does not account for neighboring elements. Furthermore, the extrapolation and nodal averaging method consistently predicts higher strain gradients across all meshes. This occurs because nodal strain values are typically higher than those at the integration points. Consequently, since the extrapolation method uses these nodal values to calculate the strain gradients, it produces larger values compared to the interpolation method, which relies on integration point strain values.

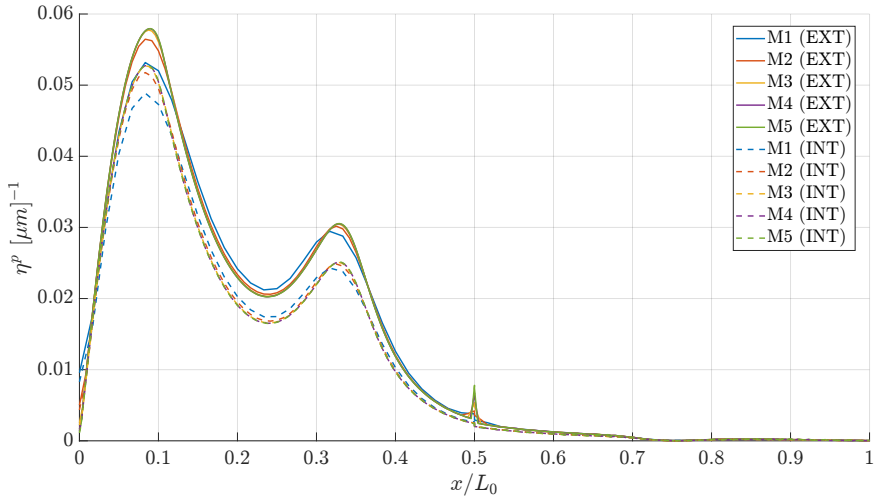

Figure 3.2: Strain gradient distribution along a path that runs through the center of the model. Dashed lines are interpolation method, solid lines extrapolation method.

Additionally, a path running through the center of the model was created to measure the strain gradients along this line. The resulting plot demonstrated in Figure 3.2 shows that mesh convergence is achieved after mesh M_3, as further refining the mesh size does not significantly alter the strain gradient distribution. In this plot, the x-axis represents the dimensionless x-coordinates, while the y-axis shows the strain gradients measured in $\mu\mathrm{m}^{-1}$. Given that the element size for M_3 was $\Delta x_3 = 12.5\,\mu\mathrm{m}$, it can be concluded that for mesh convergence, the element size must be on the same order of magnitude as the length scale parameter or smaller.

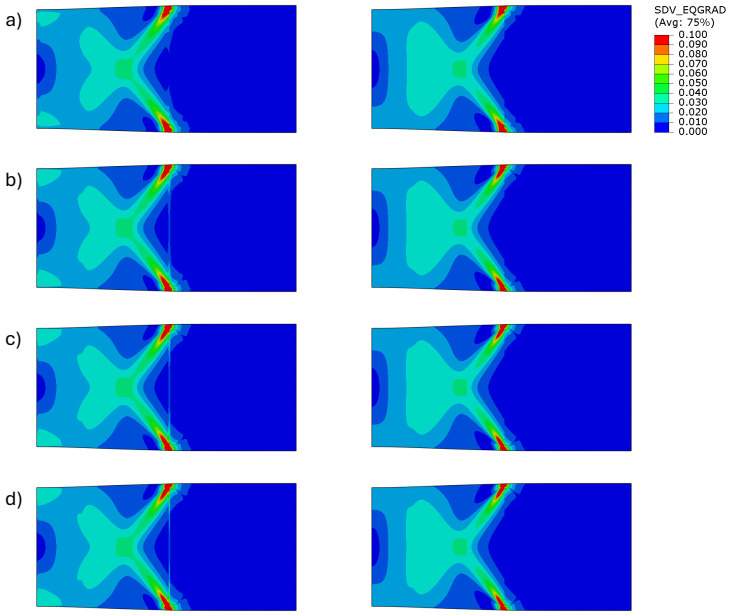

Figure 3.3: Contours of strain gradient distributions given form meshes $M2$, $M3$, $M4$, and $M5$ in a), b), c), and d) respectively. Extrapolation method on the left, interpolation method on the right.

3.2 Analysis of Wire Torsion

Wire torsion is a classical problem in strain gradient plasticity theory, where the mechanical response is highly sensitive to size effects. As the diameter of the wire decreases, the influence of strain gradients becomes more pronounced, leading to an increase in torsional stiffness that cannot be captured by conventional plasticity models. The CMSG theory is applied to model this behavior, again utilizing both the interpolation and extrapolation methods for strain gradient calculations.

This analysis investigates how these methods capture the size-dependent torsional response of microscale wires, offering insights into the strengths and limitations of each approach in predicting the enhanced material stiffness observed in small-scale structures.

Five different wire geometries are modeled, each with varying diameters, while the lengths changing accordingly. The specific dimensions for the wire diameters and lengths are provided in Table 3.2. Same material properties were used throuhout all the different wire diameters anaylsed: Young's modulus $E = 120\,\text{GPa}$, Poisson's ratio $\mu = 0.33$, initial yield stress $\sigma_y = 100\,\text{MPa}$, and the internal length scale $l = 10\,\mu m$. The hardening behaviour of the material is charactirezed by the power law with the hardening exponent $N = 0.2$. Notably. The internal length scale is kept constant across all wire cases to ensure consistency in the analysis of size effects. The mesh is kept constant across all cases, consisting of 18,240 elements, as shown in Figure 3.4. To maintain a uniform mesh, the length of each wire is chosen to be ten times the wire diameter. And for all the wire diameters, the wire is sclaed accordingly. Boundary conditions are as follows: the bottom face is fully fixed (encastre), while a torsional displacement is applied through a node that is kinematically coupled to the top surface.

Table 3.2: Wire dimensions for the analysis.

Case	W_1	W_2	W_3	W_4
Wire Radius ($a\,[\mu m]$)	6	7.5	10	85
Lenght ($L\,[\mu m]$)	120	150	200	1700

The torque (normalized with the wire diameter cubed, a^3) and twist per unit lenght (scald with wire diameter a) is represented in Figure 3.5 for copper wires of varying diameters. This demonstrates that the wires are not governed by classical continuum theory, having some sort of internal lenght scale does not allow the curves from merging into a single line, which would otherwise indicate the absence of size-dependent effects.

Figure 3.5 shows that as the wire diameter decreases, the material exhibits a stronger

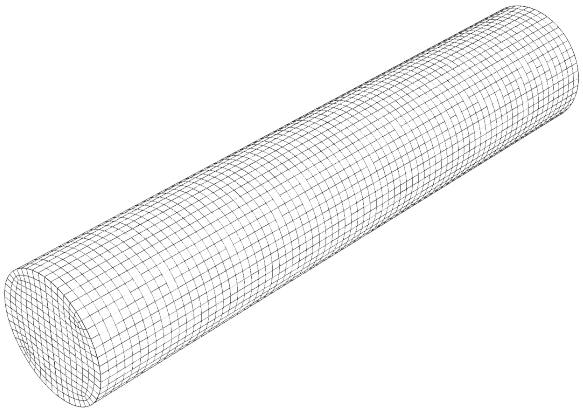

Figure 3.4: Mesh used for wire torsion problem.

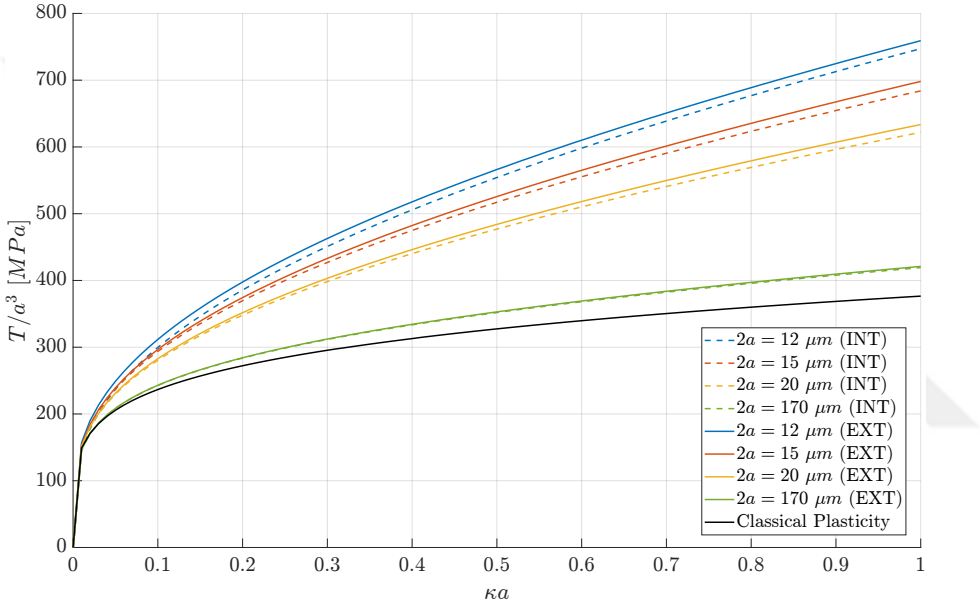

Figure 3.5: T/a^3 normalized torque, versus κa normalized twist per unit length, for wires with diameters ranging in $2a = 12, 15, 20, 170\,\mu m$, with the classical plasticty solution. The label EXT denotes results obtained using the extrapolation method, while INT denotes the interpolation method.

response, indicating size-dependent behavior. Both the interpolation and extrapolation methods predict similar trends with comparable strength levels. However, the difference between the two methods becomes more pronounced as the wire diameter decreases. This is likely due to the increasing influence of plastic strain gradients in smaller wires. Since the extrapolation method uses higher nodal values for strain gradient calculations in contrast to the lower integration point strain values, and these

strains tend to increase with decreasing wire diameter, the larger discrepancies in smaller wires can be attributed to this effect.

Although both the interpolation and extrapolation methods capture similar trends in the mechanical behavior, the strain gradient distributions show notable differences. In Figure 3.6, the strain gradient distribution for a wire with a diameter of $2a = 15\,\mu m$ is presented. In the interpolation method (a), the strain gradients form a distinct, patterned structure, while in the extrapolation method (b), the nodal averaging results in a much smoother distribution. This smoothing effect in the extrapolation method is due to the averaging of strain values at the nodes, leading to less pronounced gradient variations compared to the interpolation method.

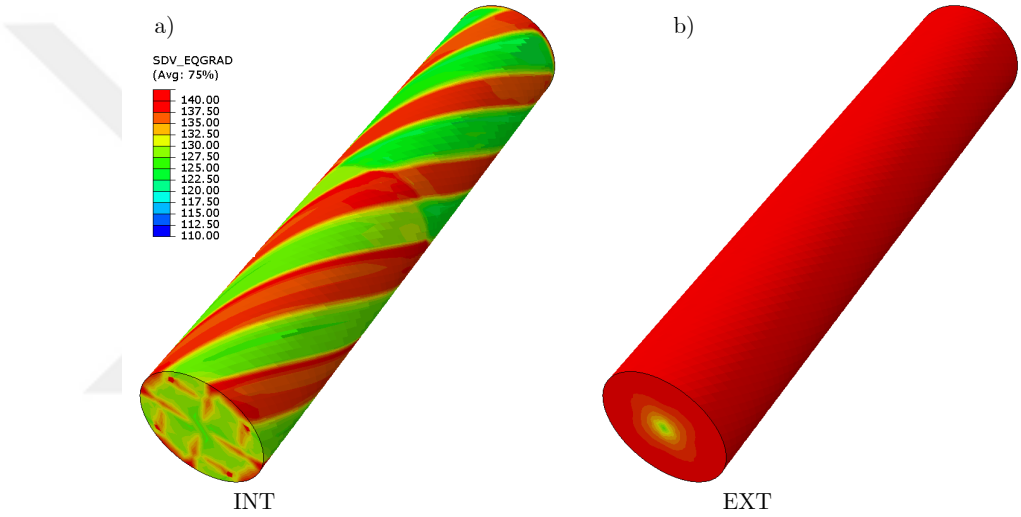

Figure 3.6: Strain gradient distributions for the wire diameter $2a = 15\,\mu m$. Interpolation method a) and extrapolation method b).

The smoothing effect introduced by the extrapolation method becomes even more apparent when examining the strain gradient distribution along the diameter of the wire. Figure 3.7 illustrates the strain gradient distribution as a function of the radial distance from the center of the wire. The extrapolation method exhibits both a higher magnitude of strain gradients and a much smoother distribution compared to the interpolation method. In contrast, the interpolation method results in more pronounced fluctuations, indicating localized variations in the strain gradients. These differences highlight the impact of nodal averaging in the extrapolation method, which tends to smooth out sharp variations, particularly in areas where the strain gradients change

rapidly across the radius.

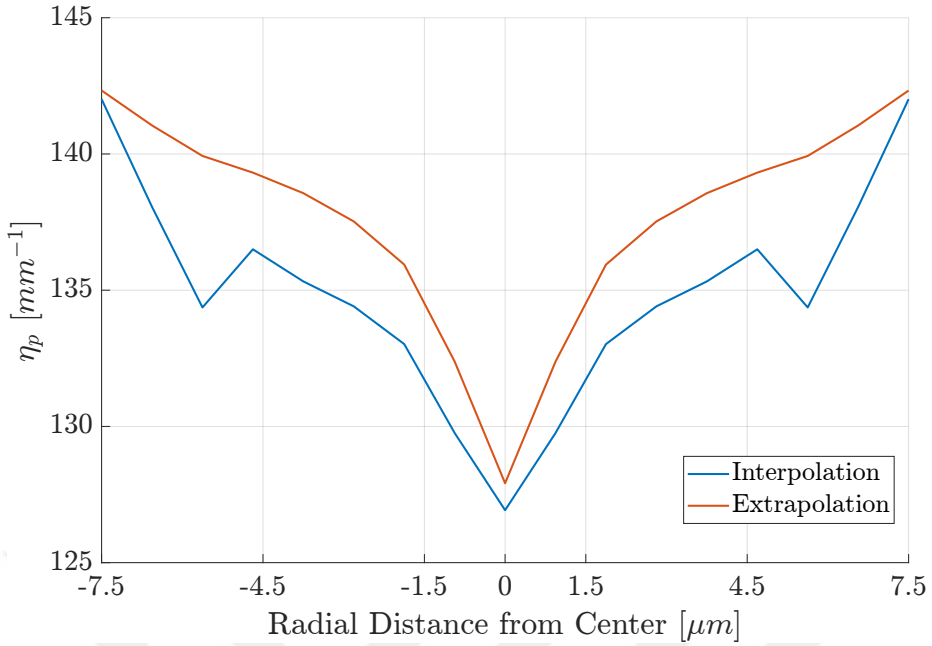

Figure 3.7: Strain gradient distribution along the radial distance from the wire center for the interpolation and extrapolation methods, wire diameter $2a = 15\,\mu m$.

The equivalent plastic strain and plastic strain gradient distributions taken from the middle section of the wire with a diameter of $2a = 15\,\mu m$ are shown in Figure 3.8. The figure compares the results from both the interpolation and extrapolation methods. In Figure 3.8a, the plastic strain gradient distribution is presented. Due to the nodal averaging scheme employed in the extrapolation method, the resulting plastic strain gradient distribution is smoother and more uniform compared to the interpolation method, which calculates gradients solely within individual elements. This smoothing effect of the extrapolation method ensures a more consistent gradient field across element boundaries, capturing the strain gradient effects more comprehensively. Such consistency can be particularly important in cases where size effects dominate the mechanical response, as strain gradients directly influence hardening behavior.

In contrast, Figure 3.8b shows the equivalent plastic strain distribution, where no significant difference is observed between the interpolation and extrapolation methods. The equivalent plastic strain, being less sensitive to the nodal averaging scheme, remains largely unaffected by the method used to calculate it. Both methods provide

a similar distribution, indicating that the strain gradient calculation primarily affects the gradient-dependent variables, while equivalent plastic strain remains stable across different calculation approaches.

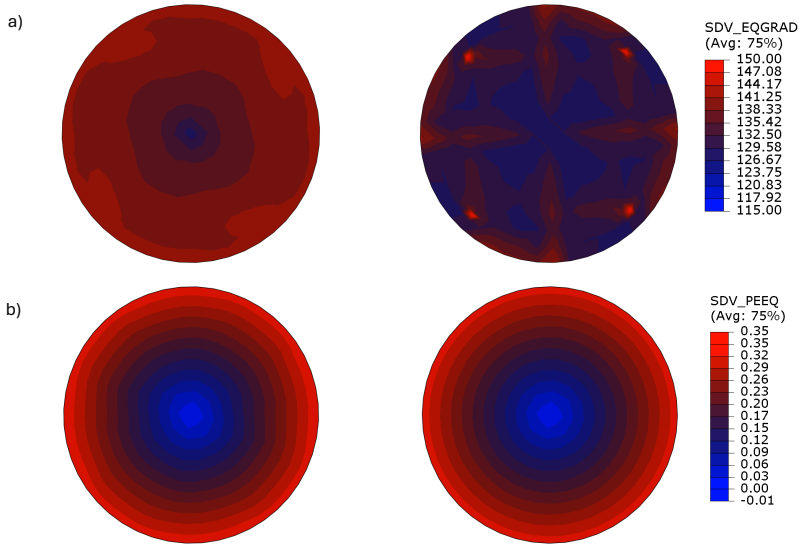

Figure 3.8: a) eqiuvalent plastic strain gradient distribution, b) equivalent plastic strain distribution alond the diameter of the wire diameter $2a = 15\,\mu m$. Extrapolation method on the left, interpolation method on the right.

Finally, the same wire models were simulated under tensile loading. The stress versus strain curves exhibited by the wires under tensional Figure 3.9 shows the stress-strain curves for wires of different diameters, comparing both the interpolation (INT) and extrapolation (EXT) methods, as well as classical plasticity. It can be observed that the stress-strain responses are nearly identical across all models, with only minimal differences between them. These differences are negligible, indicating that the strain gradient effects, which play a significant role in torsional behavior, do not have a notable impact in tensile loading, where the deformation is more uniform. Both the interpolation and extrapolation methods yield results that closely match the classical plasticity model, further suggesting that size-dependent effects are less prominent under tension.

In conclusion, similar to the study conducted by Fleck et al. (1994) it is observed that the scaled shear strength of thin copper wires increases significantly as the wire diameter decreases from 170 mm to 12 mm, with the smallest wires exhibiting a shear

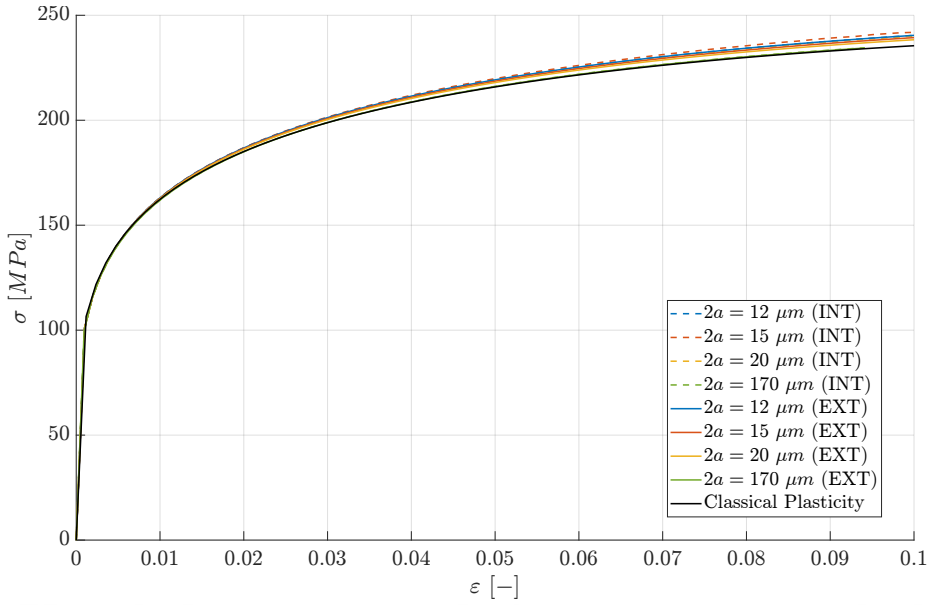

Figure 3.9: Stress-strain response for wires of varying diameters under tensile loading, comparing the interpolation (INT) and extrapolation (EXT) methods with classical plasticity.

flow strength nearly two times higher than that of the largest ones [1]. However, no size-dependent effects were seen in tension tests, which do not generate strain gradients. It is well-established that classical plasticity theories cannot explain such size-dependent effects, as they lack an intrinsic material length scale. This conclusion is reinforced by the present analysis, confirming the need for strain gradient plasticity to accurately model these behaviors.

3.3 Analysis of Particle Reinforced Composites

Metal matrix composites have known to exhibit a pronounced size effect depending on the particle size. Lloyd [11] observed that in a reinforced aluminum matrix with 15% volume fraction of silicon carbide particles, the material with smaller silicon carbide particles, measuring $7.5\,\mu m$ in diameter, demonstrated considerably greater hardening compared to those with larger particles, measuring $16\,\mu m$, despite having the same particle volume fraction. To capture this size-dependent behavior, a unit cell model, as depicted in Figure 3.10, has been developed.

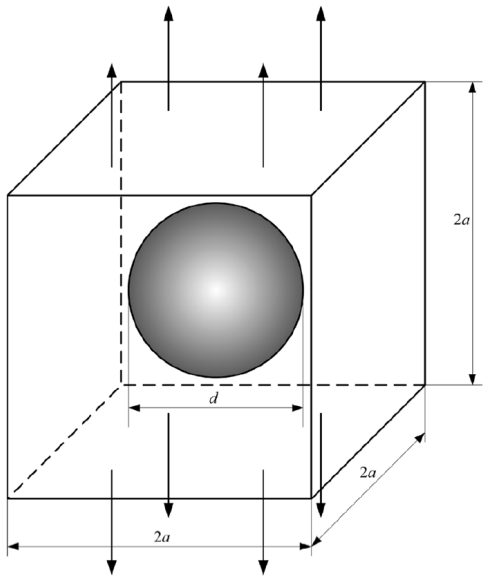

Figure 3.10: An illustration of the unit-cell in 3D with side lenghts of $2a$ and the particle diameter d.

The material properties for the aluminum matrix reinforced with silicon carbide particles are based on Lloyd's study. The silicon carbide particles are assumed to behave as isotropic linear elastic materials, with a Young's modulus of $E_{SiC} = 427\,\mathrm{GPa}$, Poisson's ratio of $\nu_{SiC} = 0.33$. The aluminum matrix, modeled using strain gradient plasticity, exhibits elastoplastic behavior. Its material properties include a Young's modulus of $E_{Al} = 76\,\mathrm{GPa}$, Poisson's ratio of $\nu_{Al} = 0.33$. For the hardening behaviour of the aluminum's matrix in uniaxial tension a power law relation is used:

$$\sigma = \sigma_{ref} f(\varepsilon^p) = \sigma_Y \left(1 + \frac{E_{Al}\varepsilon^p}{\sigma_Y}\right)^N \tag{3.1}$$

The initial yield stress of the aluminum is given as $\sigma_Y = 208\,\mathrm{MPa}$, and its stress-strain behavior follows the relation $\sigma = 464\varepsilon^{0.136}\,\mathrm{MPa}$, with the power law hardening exponent given as $N = 0.136$. The material length scale for aluminum is determined using equation (2.9). By substituting the Burgers vector value for aluminum, $b = 0.283\,\mu\mathrm{m}$, and the Taylor coefficient, $\alpha = 0.3$, the intrinsic material length scale is calculated as $l = 8.65\,\mu\mathrm{m}$.

Due to symmetry, only one-eighth of the unit cell, as shown in Figure 3.10, is modeled. This model occupies the region $0 \leq x, y, z \leq a$ in the Cartesian coordinate system, with the spherical particle centered at the origin (0,0,0). Symmetrical bound-

ary conditions are applied to the surfaces at $x = 0$, $y = 0$, and $z = 0$. While periodical boundary conditions are imposed on the surfaces at $x = a$, $y = a$, and $z = a$. These periodic conditions are enforced by linking the deformation of these surfaces to a master node, ensuring that normal displacements at each node are identical, maintaining compatibility with neighboring unit cells. A displacement δ is applied at the master node in the z-direction, with all other surfaces left traction-free, representing a uniaxial tension scenario. For the mesh, 42,779 three dimensional full integration continuum elements (C3D8) were used.

The stress-strain responses for the gradient plasticity as well as the classical plasticity theory are presented in Figure 3.11. The classical plasticity solution reasonably predicts the mechanical behavior for the matrix with particles of $16\,\mu\mathrm{m}$ diameter. However, as the particle diameter decreases, the classical plasticity model fails to capture the size-dependent hardening, since it lacks an internal length scale to account for particle size effects. The gradient plasticity theory, incorporating the length scale parameter, effectively captures the increased hardening behavior observed in the smaller particle diameter case. Additionally, the extrapolation method predicts slightly higher stress levels compared to the interpolation method, reflecting subtle differences in how each method incorporates the effects of neighboring elements.

Figure 3.12 illustrates the stress-strain curves predicted by the gradient plasticity model for various particle sizes, keeping the particle volume fraction constant at $Vf = 15\%$. As the particle diameter decreases, the model predicts increased plastic work hardening, consistent with experimental data from Lloyd [11]. Even at particle diameters of $7.5, \mu m$ and $16, \mu m$, a size effect is noticeable, and this effect becomes much more significant when the particles are reduced to around $1, \mu m$ diameter, in agreement with the findings of Nan and Clarke [116]. Furthermore, as particle size decreases, the difference between the extrapolation and interpolation methods becomes more pronounced, with larger deviations in the predicted stress levels for smaller particles.

To explore the differences between the interpolation and extrapolation methods in more detail, three different meshes were created: a coarse mesh with 1,223 elements, a medium mesh with 8,958 elements, and a fine mesh with 38,718 elements. Figure

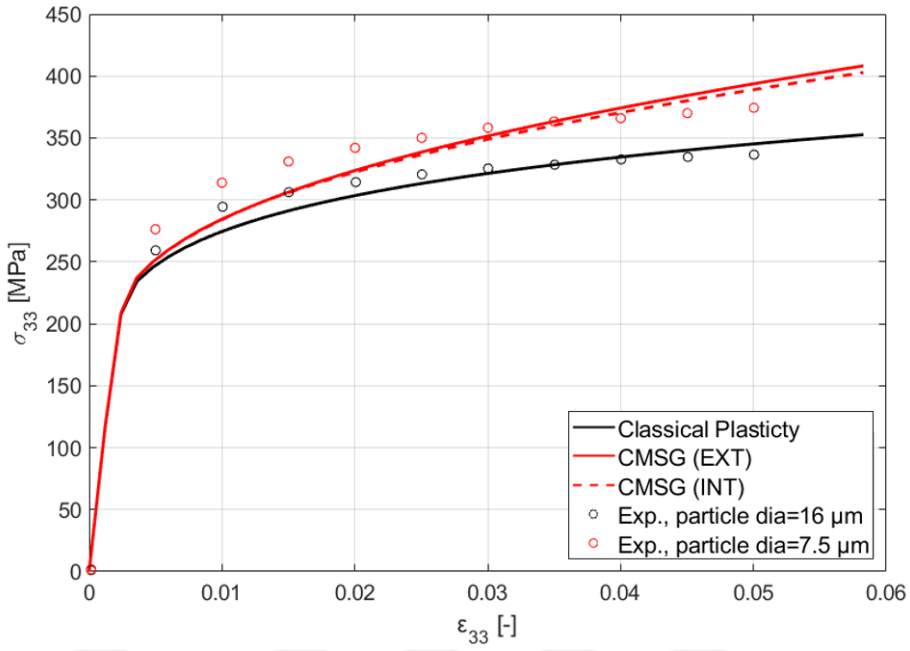

Figure 3.11: Stress-strain behaviour predicted by classical plasticty together with CMSG theory. Experiments for $16\,\mu\mathrm{m}$ and $7.5\,\mu\mathrm{m}$ diameter at 15% particle volume fraction is taken from [11].

3.13 illustrates the distribution of plastic strain gradients across these meshes.

For the extrapolation method, the strain gradient band surrounding the particle is well captured and maintained even in the coarse mesh, showing a clear localized region of high plastic strain gradients. This preservation of the gradient band suggests that the extrapolation method is better suited for capturing size effects, even with a relatively coarse discretization. As the mesh is refined, the extrapolation method continues to display these localized high-strain gradient regions, which correlate with the enhanced hardening behavior predicted by this method.

On the other hand, the interpolation method demonstrates less precision in capturing the strain gradient band, particularly in the coarse mesh, where the strain gradients are less distinct and more diffuse. As the mesh density increases, the interpolation method starts to converge towards a more accurate strain gradient distribution, but even with the fine mesh, it lacks the distinct localization seen in the extrapolation method.

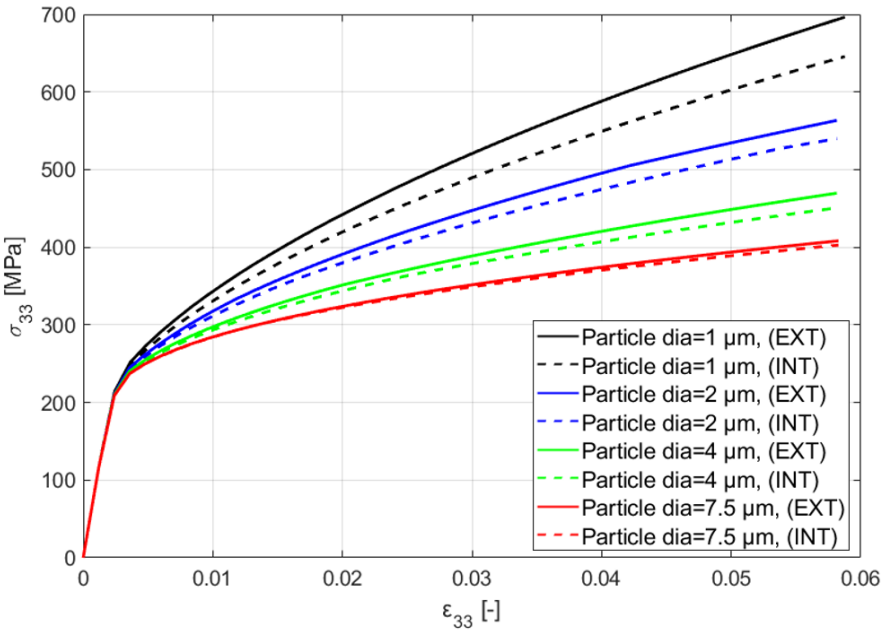

Figure 3.12: Stress versus strain plots predicted by CMSG for particle diameters $d = 1, 2, 4, 7.5\,\mu\mathrm{m}$ at 15% volume fraction, for both interpolation and extrapolation methods.

In the case of the fine mesh, both methods give similar overall distributions of strain gradients. However, the extrapolation method continues to exhibit more localized regions of high strain gradients, which explains the stronger mechanical response predicted by this method, particularly in smaller particle size scenarios. This difference between the methods becomes crucial when modeling size-dependent plasticity, as the ability to capture these localized strain gradients directly influences the accuracy of the model's predictions for hardening behavior.

3.4 Summary

In summary, this section examined the capabilities of the CMSG theory across three different problems, focusing on the effectiveness of the interpolation and extrapolation methods. Overall, the extrapolation method consistently predicts higher strain gradient levels, as it relies on nodal strain values to calculate the gradients. This leads to a stronger material response. In the case of interfaces between two different mate-

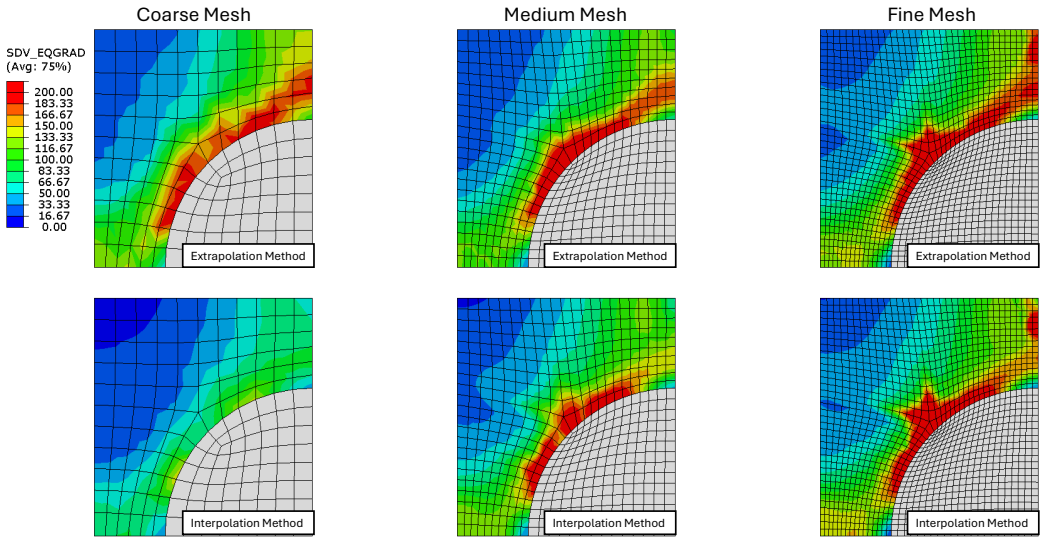

Figure 3.13: Plastic strain gradient distributions for coarse, medium, and fine meshes using the extrapolation and interpolation methods.

rials, the extrapolation method successfully captures the strain gradients that develop at the boundary, while the interpolation method falls short in this aspect.

Additionally, the extrapolation method provides smoother and more continuous strain gradient distributions, as demonstrated in the wire torsion problem. Another advantage of this method is its ability to predict localized regions of high strain gradients, as seen in the particle-reinforced composite example.

On the other hand, the interpolation method is easier to implement, runs faster, and can capture trends similar to the extrapolation method with sufficient mesh resolution. However, for higher accuracy and more detailed gradient localization, the extrapolation method proves to be superior. In summary, while the interpolation method offers a faster, more efficient approach, the extrapolation method delivers greater accuracy, particularly in problems requiring the resolution of localized strain gradients

CHAPTER 4

NONLOCAL DAMAGE MODEL BASED ON CMSG THEORY

In this section, the current framework is extended to incorporate a nonlocal damage law, taken from the work of Mediavilla et al. [90]. This nonlinear damage law governs damage evolution using effective stress and equivalent plastic strain. While several variables could be regularized within the CMSG theory, the equivalent plastic strain $\varepsilon_{eq} = \sqrt{\frac{2}{3}\varepsilon^p_{ij}\varepsilon^p_{ij}}$ is a natural choice, as it directly influences both the plasticity and damage components. Therefore, it is selected as the nonlocal variable. To enforce nonlocality, an integral-type weighted averaging scheme is applied.

4.1 Integral-type Nonlocal Averaging

Nonlocal constitutive theories arise from the recognition that the material's local state at a specific point may not be sufficient or accurate for determining the stress at that location. This occurs because, at sufficiently small scales, materials deviate from behaving as continuous media, resulting in noticeable effects due to heterogeneity and discontinuous microstructures. For metals, this critical scale is typically in the micron range. When the strain distribution is relatively smooth, as is typically the case during elastic deformation, standard local theories can offer a good approximation with minimal deviation from the actual material behavior. However, when strain localization occurs, the characteristic wavelength of the deformation field shortens significantly, activating nonlocal effects [117]. As a result, nonlocal theories aimed at resolving localization issues often neglect nonlocal elastic effects and instead concentrate on applying nonlocal averaging to dissipative processes linked to an internal variable. For example in plasticity, this internal variable is typically a softening variable, such

as plastic strain or equivalent plastic strain.

The local variable ε_d, is used to derive its nonlocal counterpart $\bar{\varepsilon}_d$ for an arbitrary material point $\mathbf{x}$ can be obtained in the current configuration through the nonlocal evolution equation.

$$\bar{\varepsilon}_d = \frac{1}{W(\mathbf{x})} \int_V w(\mathbf{x} - \mathbf{y}) \varepsilon_d(\mathbf{y})\, dV \tag{4.1}$$

With, V representing the current volume of the domain, and the positional vector denoted as $\mathbf{x}$, and $\mathbf{y}$. The weight function used in this thesis w, is taken from the study conducted by Tvergaard and Needleman [118], and is given explicitly by:

$$w(z) = \left[\frac{1}{1 + \left(\frac{z}{L}\right)^{p_w}} \right]^{q_w} \tag{4.2}$$

Where $z = \sqrt{\mathbf{z} \cdot \mathbf{z}}$, is the norm of the poisition vector and $\mathbf{z} = \mathbf{x} - \mathbf{y}$ represents the positional distance between neighboring integration points in the domain of the current configuration. Here, L is termed as the nonlocal material characteristic length which takes positive definite values. $p_w = 8$ and $q_w = 2$ are mathematical constants that dictate w which controls how intense the nonlocal enchancement will be as given in equation (4.2). the weight function w is constructed such that if the distance away from that point is large the weight is close to zero, whereas, for a comparable values of z and L wieht has a value close to unity. Figure 4.1, illustrates this a relatively narrow transition region exists between these states. Specifically, w equals 0.25 at $z/L = 1.0$, 0.021 at $z/L = 1.25$, and 0.0014 at $z/L = 1.5$. In the computations, a cutoff length $L_c = 1.5L$ is applied, setting w in equation (4.2) to zero for $z > L_c$. This weight function is then integrated over the full domain as following:

$$W(\mathbf{x}) = \int_V w(\mathbf{x} - \mathbf{y})\, dV \tag{4.3}$$

The limit for $L \to 0$ represents the local formulation where no nonlocal effects are seen. For $L > 0$, the condition $\bar{\varepsilon}_d \equiv \varepsilon_d$ is satisfied only if ε_d is spatially uniform, meaning nonlocality is inherently linked to spatial gradients in $\bar{\varepsilon}_d$.

4.2 Damage Law

Ductile damage is generally recognized as a mechanism driven by plastic deformation. In this thesis, the damage evolution equation proposed by Mediavilla et al. [90]

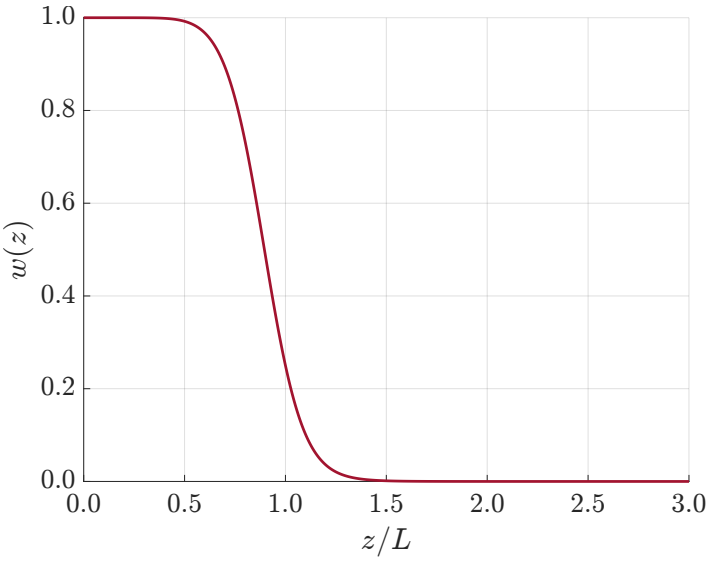

Figure 4.1: Weight function given in equation (4.2) with $p_w = 8$ and $q_w = 2$.

is adopted, selecting the equivalent plastic strain ε_{eq} as the damage variable ε_d to be enhanced nonlocally. Although other choices are available—such as the volumetric plastic strain used as the damage variable (see [119]) or defining ε_d as the local damage variable itself (see [120, 121]). However as expected, not all approaches yield satisfactory results. The following modification is made to the nonlocal counterpart $\bar{\varepsilon}_d$ for $\varepsilon_d = \varepsilon_{eq}$ the damage driving variable,

$$\dot{\varepsilon}_d = \begin{cases} 0, & \varepsilon_{\text{eq}} < \varepsilon_i(\sigma) \\ \dot{\varepsilon}_{\text{eq}}, & \text{once } \varepsilon_{\text{eq}} \geq \varepsilon_i(\sigma) \text{ during loading history.} \end{cases} \tag{4.4}$$

Where damage is assumed to start accumulating at ε_i which is termed as the damage initiation strain. Consequently, the initiation of the damage is inherently controlled by the equivalent plastic strain ε_{eq}. Further, healing effects are prevented by enforcing Kuhn-Tucker loading-unloading conditions with an additional history variable κ:

$$\dot{\kappa} \geq 0, \quad \dot{\kappa}(\bar{\varepsilon}_d - \kappa) = 0, \quad \bar{\varepsilon}_d - \kappa \leq 0. \tag{4.5}$$

Therefore, κ is associated with the non-local variable $\bar{\varepsilon}_d$ under certain constraints. The evolution of damage depends on the additional variable κ:

$$\dot{D} = h_D(D)\dot{\kappa} \tag{4.6}$$

Damage law is taken from the literature, [91, 122].

$$h_D(D) = D_c \frac{3}{\tanh(3)\varepsilon_c} \left(1 - \tanh^2(3)(2D-1)^2\right). \tag{4.7}$$

Or in the integrated form:

$$D = \frac{D_c}{2}\left(1 + \frac{1}{\tanh(3)} \tanh\left(\frac{6\kappa}{\varepsilon_c} - 3\right)\right), \tag{4.8}$$

The shape of the damage law can be seen in 4.2. Where previously introduced variables for damage initiation strain ε_i, and critical strain ε_c is shown. Equation (4.7) causes damage to grow slowly at the start and end, which can be more stable in calculations because there are no sudden jumps in damage growth. The material assumed to be intact for $\kappa = 0$ and reaches complete failure when $\kappa = \varepsilon_c$. Thus, full material failure occurs at a specific value rather than asymptotically. Complete failure is defined by $D = D_c = 1$.

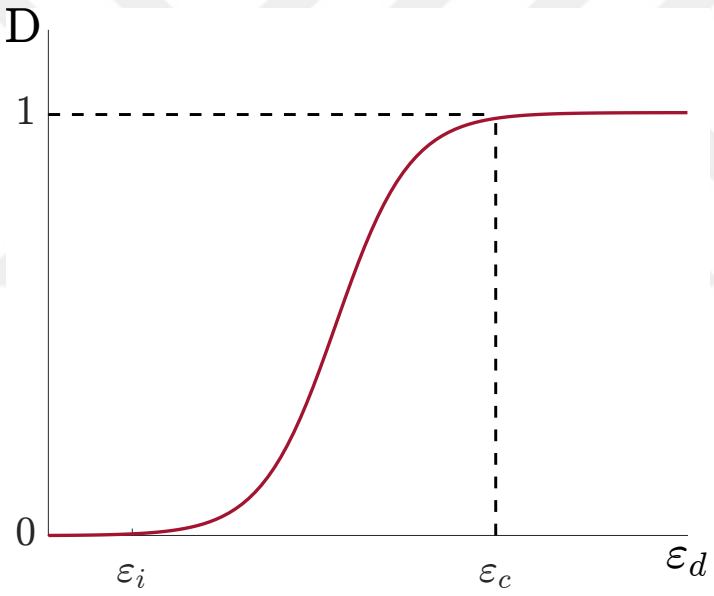

Figure 4.2: Non-linear damage evolution law dictated by equation (4.2).

4.3 Modification of CMSG Considering Damage Effects

From the continuum damage theory [63], the yielding criterion considering the damage effects can be written as:

$$\hat{f} = \hat{\sigma}_e - \sigma_{flow} = \frac{\sigma_e}{1-D} - \sigma_{flow} = 0 \tag{4.9}$$

Where σ_e and $\hat{\sigma}_e$ denote the effective stresses in undamaged and damaged states respectively. Therefore, from equation (4.9), the flow stress equation of CMSG plasticity (2.8), can be re-written as:

$$\sigma_e = (1-D)\sigma_{flow} = \sigma_Y \sqrt{(1-D)^2 f^2(\varepsilon^p) + \bar{l}\eta^p} = \bar{\sigma}_{flow} \tag{4.10}$$

In which $\bar{l}$ is the degraded length scale parameter which takes the form of:

$$\bar{l} = 18\alpha^2 \left(\frac{\bar{\mu}}{\sigma_{ref}}\right) b = (1-D)^2 18\alpha^2 \left(\frac{\mu}{\sigma_{ref}}\right) b = (1-D)^2 l \tag{4.11}$$

From the above equation, it can be inferred that as the damage increases, the material intrinsic length scale becomes smaller. Moreover, the flow stress is both affected by the strain gradient and microstructural damage. Here a competition of mechanisms can be observed. On one hand, the strain gradient causes hardening in the material, however, on the other hand, damage leads to softening of the plastic flow stress.

By incorporating a damage mechanism into the CMSG theory, it is possible to account for the effects of microstructural defects, such as voids or cracks. This modification expands the framework to consider not only dislocations but also the initiation and evolution of these damage.

Starting from the definition of the yield function in accordance with J_2 flow theory, the plastic strain of a degraded material can be expressed by the modification of equation (2.29):

$$\dot{\boldsymbol{\varepsilon}}^p = \frac{\partial \hat{f}}{\partial \sigma'_{ij}} \dot{\lambda} = \frac{1}{1-D} \frac{3\sigma'_{ij}}{2\sigma_e} \dot{\lambda} \tag{4.12}$$

where $\hat{f}$ represents the yield criterion for a damaged material, and $\dot{\lambda}$ is the plastic multiplier, which is related to the equivalent plastic strain $\dot{\varepsilon}^p$ as:

$$\dot{\varepsilon}^p = \sqrt{\frac{2}{3}\dot{\varepsilon}^p_{ij}\dot{\varepsilon}^p_{ij}} = \frac{1}{1-D}\dot{\lambda} \tag{4.13}$$

Additionally, using equation (2.17), the equivalent plastic strain rate $\dot{\varepsilon}^p$ in the presence of damage can be expressed as:

$$\dot{\varepsilon}^p = \dot{\varepsilon}\left[\frac{\sigma_e}{\bar{\sigma}_{flow}}\right]^m = \dot{\varepsilon}\left[\frac{\sigma_e}{\sigma_Y\sqrt{(1-D)^2 f^2(\varepsilon^p) + \bar{l}\eta^p}}\right]^m \tag{4.14}$$

Combining equations (4.12)-(4.14) with the relations $\bar{K} = (1-D)K$ and $\bar{\mu} = (1-$

$D)\mu$, along with the constitutive equation provided in (2.19), results in:

$$\dot{\sigma}_{ij} = (1-D)K\dot{\varepsilon}_{kk}\delta_{ij}$$
$$+2(1-D)\mu\left[\dot{\varepsilon}'_{ij} - \frac{3\dot{\varepsilon}}{2\sigma_e}\left(\frac{\sigma_e}{\sigma_Y\sqrt{(1-D)^2 f^2(\varepsilon^p)+\bar{l}\eta^p}}\right)^m \sigma'_{ij}\right] \tag{4.15}$$

This completes the constitutive relation for the CMSG theory with damage.

4.3.1 Derivation of the Tangent Stiffness Matrix With Damage Effects

This section details the derivation of the material stiffness matrix needed to implement the current framework into an ABAQUS user material subroutine (UMAT). We begin by applying the degradation to the shear modulus in equation (2.32):

$$\left(1+\frac{3(1-D)\mu}{\sigma_e}\Delta\varepsilon^p\right)\sigma'_{ij} = 2\mu(1-D)\hat{e}_{ij} \tag{4.16}$$

Following the principles introduced in Chapter 2, we rearrange equation (4.16) as:

$$\sigma_e + 3(1-D)\mu\Delta\varepsilon^p = 3(1-D)\mu\tilde{e} \tag{4.17}$$

Substituting equation (4.14), we arrive at:

$$\sigma_e - 3(1-D)\mu\left(\tilde{e} - \Delta\varepsilon\left(\frac{\sigma_e}{(1-D)\sigma_{flow}}\right)^m\right) = 0 \tag{4.18}$$

Newton's method can be used to solve this equation:

$$\sigma_e = \sigma_e + \frac{3(1-D)\mu\left(\tilde{e} - \Delta\varepsilon\left(\frac{\sigma_e}{(1-D)\sigma_{flow}}\right)^m\right) - \sigma_e}{1+3(1-D)\mu h} \tag{4.19}$$

where the modified h is given by:

$$h = m\Delta\varepsilon\left(\frac{\sigma_e}{(1-D)\sigma_{flow}}\right)^{m-1}\frac{1}{\sigma_{flow}} \tag{4.20}$$

Once convergence is achieved, the effective plastic strain increment can be determined from:

$$\Delta\varepsilon^p = \tilde{e} - \frac{\sigma_e}{3(1-D)\mu} \tag{4.21}$$

The deviatoric stress σ'_{ij} and plastic strain increment $\Delta\varepsilon^p_{ij}$ can be calculated using equations (4.12) and (4.16), respectively. Taking the variation of equation (4.16)

results in:

$$\left(1+\frac{3(1-D)\mu}{\sigma_e}\Delta\varepsilon^p\right)\partial\sigma'_{ij}+\sigma'_{ij}\frac{3(1-D)\mu}{\sigma_e}\left(\partial\Delta\varepsilon^p-\frac{\Delta\varepsilon^p}{\sigma_e}\partial\sigma_e\right) = 2(1-D)\mu\partial\hat{e}_{ij} \tag{4.22}$$

Similarly, the variation of equation (4.17) is:

$$\partial\sigma_e+3(1-D)\mu\partial\Delta\varepsilon^p=3(1-D)\mu\partial\tilde{e} \tag{4.23}$$

Considering the definition of $\tilde{e}$ leads to:

$$\partial\sigma_e=\frac{2}{3\tilde{e}}\frac{3(1-D)\mu}{1+3(1-D)\mu h}\hat{e}_{ij}\partial\hat{e}_{ij} \tag{4.24}$$

Substituting back into equation (4.22) and rearranging yields:

$$\partial\sigma'_{ij}=\left(\frac{2\sigma_e}{3\tilde{e}}I_{ijkl}-\frac{1}{\sigma_e\tilde{e}}\left(h-\frac{\Delta\varepsilon^p}{\sigma_e}\right)\frac{3(1-D)\mu}{1+3(1-D)\mu h}\sigma'_{ij}\sigma'_{kl}\right)\partial\hat{e}_{kl} \tag{4.25}$$

where $I^{(4)}_{ijkl}$ is the fourth-order unit tensor. Thus, by considering the relationship between the stress and strain tensors and their deviatoric components, the consistent material Jacobian can be expressed as:

$$\begin{aligned}\partial\sigma_{ij}=&\left(\frac{2\sigma_e}{3\hat{\varepsilon}}I^{(4)}_{ijkl}+\left((1-D)K-\frac{2\sigma_e}{9\tilde{e}}\right)I_{ij}I_{kl}\right.\\&\left.-\frac{1}{\sigma_e\tilde{e}}\left(h-\frac{\Delta\varepsilon^p}{\sigma_e}\right)\frac{3(1-D)\mu}{1+3(1-D)\mu h}\sigma'_{ij}\sigma'_{kl}\right)\partial\varepsilon_{kl}\end{aligned} \tag{4.26}$$

This provides the tangent stiffness matrix. Note that in the undamaged state (i.e., $D=0$), the above expression simplifies to the same relation as given in equation (2.44).

4.4 Finite Element Implementation

The nonlocal damage model is implemented as an additional option to the existing user material subroutine, where the equivalent plastic strain, serving as the nonlocal variable, is updated incrementally:

$$(\bar{\varepsilon}_{eq})_{n+1}=(\bar{\varepsilon}_{eq})_n+\Delta(\bar{\varepsilon}_{eq})_{n+1} \tag{4.27}$$

Here, $\Delta(\bar{\varepsilon}_{eq})_{n+1}$ is calculated using equations (4.12)–(4.15). At each increment, the UEXTERNALDB subroutine determines distances between integration points from

stored coordinates, facilitating the global averaging scheme. Meanwhile, the UMAT subroutine computes the total plastic strain ε^p, calculates the equivalent plastic strain ε_{eq}, and stores these values in a global array. This staggered approach uses equivalent plastic strains from the previous increment, making a small time increment crucial for accurate results.

4.5 Shear Band Specimen

The formation of shear bands is examined with this example. The length scale parameter controlling the nonlocal regularization L is kept constant while decreasing the element size. The geometry of the specimen is shown in Figure 4.3, and the material properties are listed in Table 4.1. The material parameters are specifically selected to trigger the formation of a single inclined shear band.

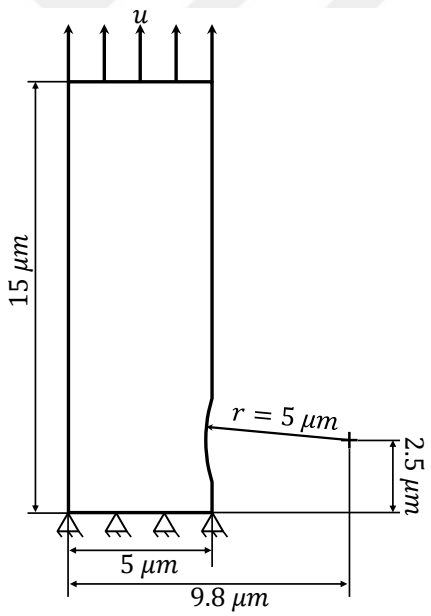

Figure 4.3: Geometry and boundary conditions of shear band specimen.

Figure 4.4 presents the global response of the shea band specimen simulated with the nonlocal damage coupled with CMSG model under various levels of mesh refinement. In these simulations, the parameter b_e represents the mesh size, while L is the characteristic length that governs the nonlocal damage regularization. The figure illustrates the normalized force-displacement behavior as the mesh becomes finer, with a focus

on how the nonlocal damage model affects the force response during strain-softening.

The normalized force F is determined by the equation $F = A_0/\sigma_Y$, where A_0 refers to the initial, undeformed cross-sectional area measured at the geometrical imperfection, and σ_Y denotes the material's yield stress. This formulation allows for a consistent comparison of force responses across different simulations. On the other hand, the normalized displacement u/H_0 is defined as the ratio of the applied displacement u to the initial height H_0 of the specimen.

Table 4.1: Material parameters for shear band specimen.

CMSG Parameters	E [GPa]	ν	σ_Y [MPa]	l [μm]
	80	0.33	150	1
Damage Parameters	ε_c	L [mm]		
	0.25	0.0005		

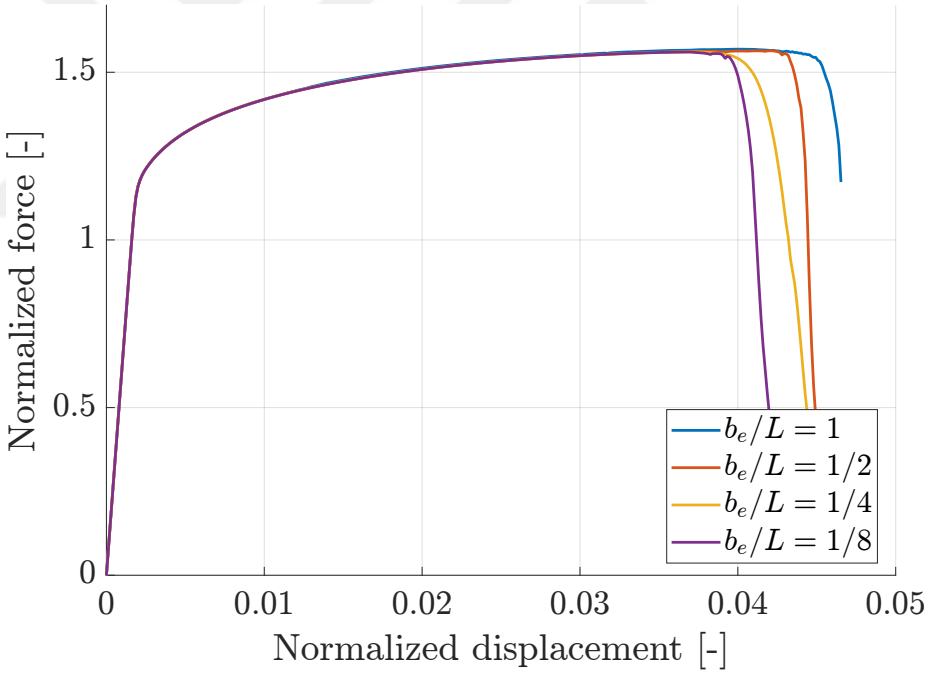

Figure 4.4: Dimensionless force vs. displacement curve for shear band specimen.

Figure 4.5 shows the fully fractured state with the development of a shear band for different mesh refinements, where the ratio of the element size to the length scale, b_e/L, ranges from 1 to 1/8. As a nonlocal regularization scheme is applied, the width of the shear band remains consistent despite mesh refinement, demonstrating that the

model is not sensitive to the mesh size. This consistency across mesh sizes highlights the robustness of the nonlocal approach in preventing shear band localization from being overly dependent on the element size. The figure further emphasizes that applying a nonlocal regularization ensures the proper capturing of strain localization phenomena, making the model more reliable for predicting shear band formation and progression in various mesh configurations.

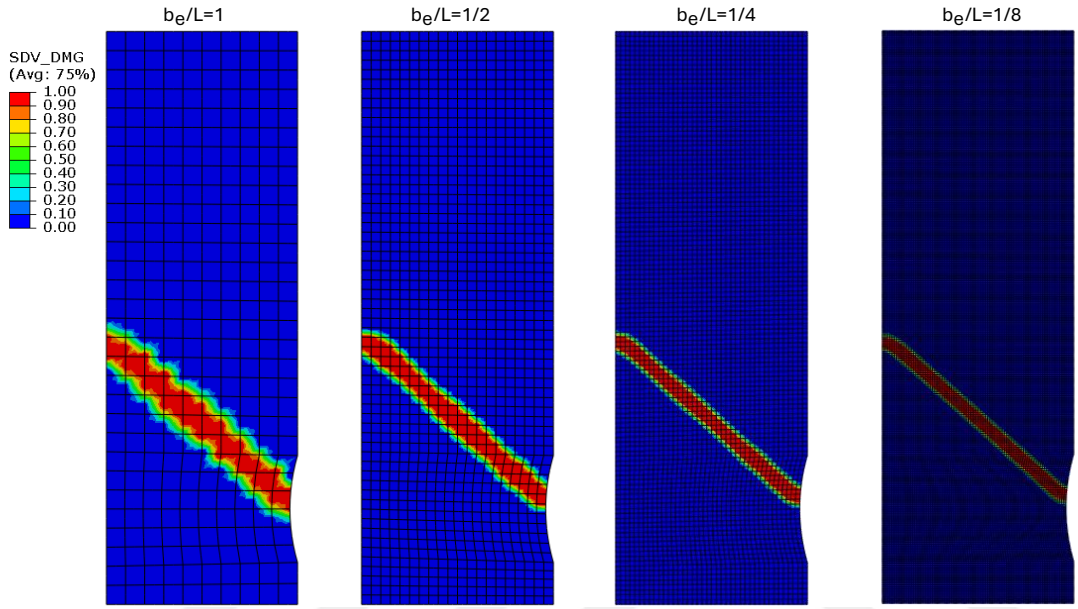

Figure 4.5: Damage distribution at the fractured states.

CHAPTER 5

APPLICATIONS OF CMSG THEORY COUPLED WITH DAMAGE

This chapter presents the application of the CMSG theory coupled with nonlocal damage to a range of problems. The performance of the damage model is assessed through both small-scale and large-scale yielding scenarios, with a focus on its ability to predict size-dependent behavior and damage-related phenomena. The first example examines Mode I crack tip fields, representing a sharp crack in a small-scale yielding problem. The second problem continues with small-scale yielding, focusing on a compact tension specimen. The final case explores an asymmetric double-notch specimen where a blunt defect initiates the formation of shear bands.

The results reveal that for sharp cracks, where stresses and strains are highly localized, the strain gradient effect leads to elevated stresses, which in turn accelerates crack formation. In contrast, for cases like the asymmetric double-notch specimen, where damage is driven by the localization of plastic flow, increasing the plastic length scale delays the onset of damage by diffusing the localization. These examples illustrate the versatility of the CMSG theory in capturing both size effects and damage progression across different geometries and loading conditions.

5.1 Analysis of Damage on Mode I Crack Tip Fields

The analysis of crack-tip fields is conducted through a boundary-layer formulation integrated within the finite element method. The crack region is represented within a circular domain, where mode-I loading is applied at the outer boundary via specified

displacements as detailed below:

$$u(r,\theta) = K_I \frac{1+\nu}{E}\sqrt{\frac{r}{2\pi}}\cos\left(\frac{\theta}{2}\right)(3-4\nu-\cos\theta)\,, \tag{5.1}$$

$$v(r,\theta) = K_I \frac{1+\nu}{E}\sqrt{\frac{r}{2\pi}}\sin\left(\frac{\theta}{2}\right)(3-4\nu-\cos\theta)\,, \tag{5.2}$$

Horizontal u and vertical V displacements are given above. A cylindrical datum system is placed at its origin, which coincides with the global datum system. E idenotess, Young's modulus, ν is Poisson's ratio, and K_I is the stress intensity factor representing the applied load.

Half of the circular domain is modeled due to the symmetry with which plane strain conditions are assumed. The outer radius is set to $R = 42\,\mathrm{mm}$, and the model is discretized using 1,730 fully integrated, four-noded quadrilateral plane-strain elements (CPE4). As shown in Figure 5.1, a fine mesh is applied near the crack tip, where the smallest element size is approximately $10\,\mathrm{nm}$, ensuring accurate resolution of strain gradient effects near the crack tip. Material properties are given in Table 5.1.

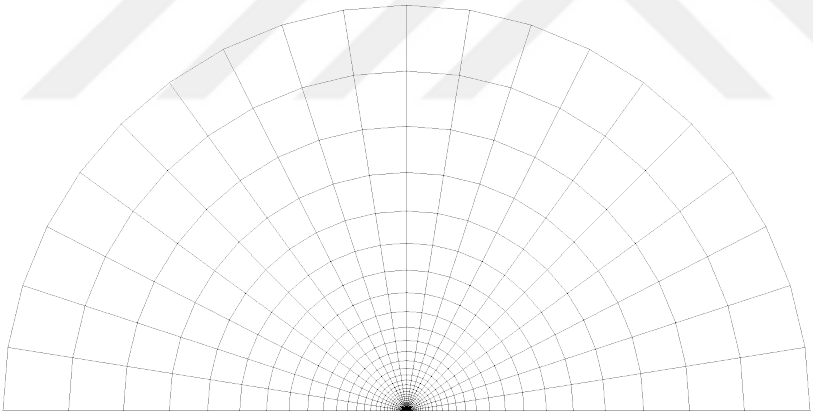

Figure 5.1: Mesh used for the crack tip fields.

Table 5.1: Material parameters for used for crack tip fields.

CMSG Parameters	$E\,[\mathrm{GPa}]$	ν	$\sigma_Y\,[\mathrm{MPa}]$	$l\,[\mu\mathrm{m}]$
	100.	0.33	200.0	3.53
Damage Parameters	ε_c	$L\,[\mu\mathrm{m}]$		
	0.6	0.04		

Figure 5.2 presents a log-log plot of the normalized hoop stress $\sigma_{\theta\theta}$ distribution ahead of the crack tip ($\theta = 0°$), subjected to a remote load of $K_I = 17.3\sigma_Y\sqrt{l}$. The results are provided for the CMSG plasticity model, both with and without damage, as well as for the classical plasticity solution. The hoop stress $\sigma_{\theta\theta}$ is normalized by the material yield strength, and the distance to the crack tip r spans from $0.1\,\mu\mathrm{m}$ to $200\,\mu\mathrm{m}$, covering both the near-tip region where strain gradients dominate and the farther field where traditional HRR field predictions apply.

As depicted in the figure, the stress fields predicted by the CMSG theory align well with the Hutchinson, Rice, and Rosengren (HRR) predictions at distances further from the crack tip, validating the consistency of the model in areas dominated by classical plasticity theory. However, in regions closer to the crack tip (within a $1,\mu\mathrm{m}$ distance), the strain gradient effects become significant, causing a notable elevation in stress. At $r = 0.1\,\mu\mathrm{m}$, the CMSG model predicts hoop stresses reaching $11.2\sigma_Y$, much higher than the classical plasticity prediction of $7.5\sigma_Y$. These elevated stress levels, as suggested by Qu et al. [123], are sufficient to trigger cleavage fracture, underscoring the importance of considering strain gradient effects in predicting failure near crack tips.

The inclusion of damage in the CMSG model introduces softening effects, leading to stress predictions that fall between those of the classical plasticity and CMSG without damage cases. The damage-modified CMSG model illustrates how nonlocal damage mechanisms can moderate the stress concentrations predicted by gradient plasticity, although the stress levels remain significantly higher than those predicted by classical plasticity alone. This interplay between strain gradient hardening and damage softening is crucial for capturing more realistic stress distributions near crack tips, particularly in the context of size-dependent behavior.

Overall, this figure underscores the critical role of strain gradient plasticity in predicting high-stress concentrations near crack tips that cannot be captured by classical plasticity models. The ability to incorporate both strain gradients and damage within the same framework allows for a more comprehensive understanding of material behavior under fracture conditions, particularly in scenarios where size effects are prominent.

Figure 5.3a illustrates the equivalent plastic strain gradient distribution near the crack tip for both $l = 0$ and $l = 3.53\,\mu\text{m}$. In both cases, the strain gradient is highly localized around the crack tip, reflecting the intense deformation occurring in this region. For the case of $l = 3.53\,\mu\text{m}$, the strain gradients are more concentrated, emphasizing the influence of the length scale on the gradient localization. This localization is crucial as it contributes to the overall hardening behavior, which would not be captured in the $l = 0$ case (classical plasticity) without the inclusion of strain gradient effects.

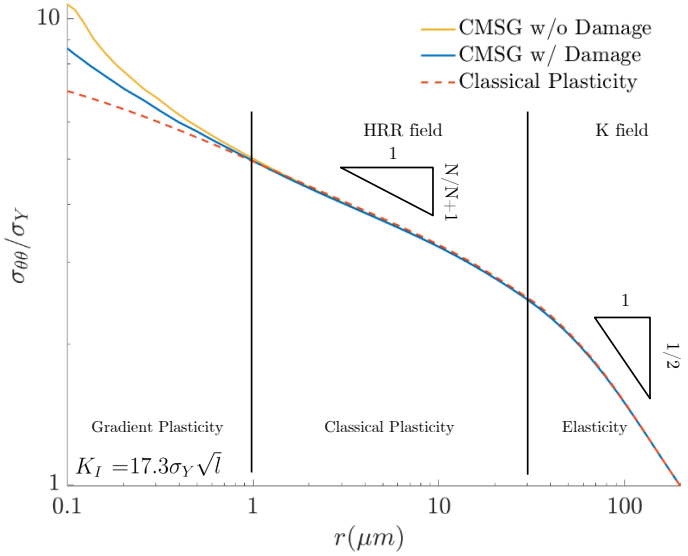

Figure 5.2: Normalized hoop stress $\sigma_{\theta\theta}$ vs the distance from the crack tip.

Figure 5.3b shows the von Mises stress distribution near the crack tip. In both cases, stress concentrations are observed at the crack tip, but for $l = 3.53\,\mu\text{m}$, the stress levels are reduced compared to $l = 0$. This reduction is primarily due to the accumulation of damage, which softens the material and leads to a more distributed stress field. The presence of nonlocal damage in the $l = 3.53\,\mu\text{m}$ case limits the stress build-up, resulting in delayed crack propagation and potentially postponing failure. The difference in stress distribution between the two cases highlights the interplay between hardening due to strain gradients and softening due to damage accumulation.

Overall, the figures clearly illustrate the critical role of the length scale in capturing the size-dependent effects near the crack tip, influencing both the strain gradient and stress fields in regions of high deformation.

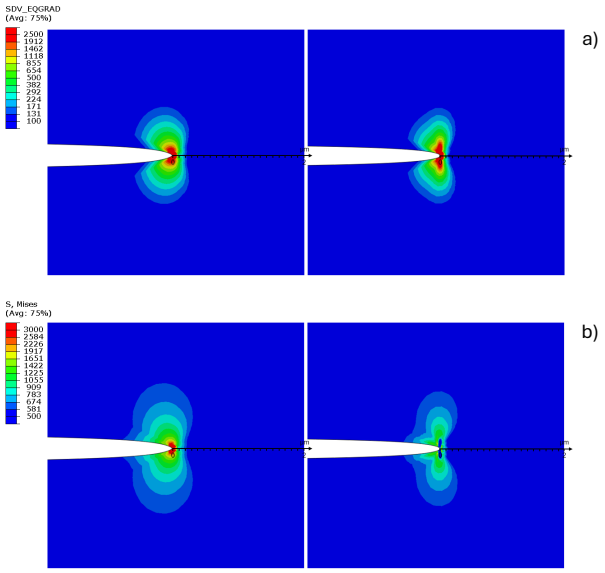

Figure 5.3: Contour plots near the crack tip a) equivalent plastic strain gradient distribution, b) von Mises stress distribution near the crack (left $l = 0$, right $l = 3.53\,\mu\text{m}$).

5.2 Analysis of Compact Tension Sample

A micro-sized compact tension specimen is simulated, with the geometry and mesh depicted in Figure 5.4. Approximately 27,000 quadrilateral linear finite elements (CPE4) are used. For the boundary conditions, a vertical displacement is applied to the top pin while it is constrained in the horizontal direction. This displacement is imposed through a reference point, kinematically coupled to the surface of the top pin. Meanwhile, the bottom pin is fixed in both the vertical and horizontal directions. The material is modeled with linear hardening. Consequently, the power law hardening described in equation (2.6) is replaced by the following relationship:

$$\sigma = \sigma_Y f(\varepsilon^p) = \sigma_Y \left(1 + \frac{\varepsilon^p E_t}{\sigma_Y}\right)$$

where $E_t = 714.8\,\text{MPa}$ represents the plastic linear hardening modulus. The elasticity-related material properties include $E = 71.48\,\text{GPa}$, $\nu = 0.3$ for Young's Modulus and Poisson's ratio, respectively. The plasticity-related material parameters read: and an initial yield stress of $\sigma_Y = 345\,\text{MPa}$. The critical strain, $\varepsilon_c = 0.05$, represents the point of complete material failure.

The length scale parameter, L, which governs the nonlocal regularization, is chosen

to be $8\,\mu\mathrm{m}$, four times the element size near the crack tip. This ensures the average element size around the crack tip is $\Delta x = 2\,\mu m$, providing the necessary resolution to achieve converged results.

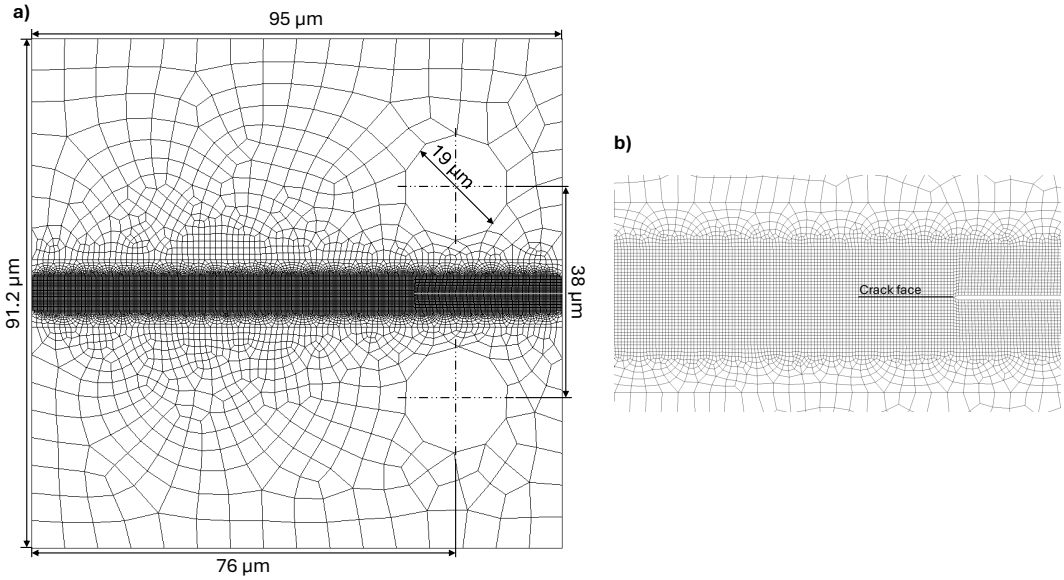

Figure 5.4: a) Geometry together with the mesh of the compact tension specimen, b) closeup image of the crack face and crack tip.

Four different models were created with the same geometries, differing only in the internal length scale parameter l. The contour plots in Figure 5.5 show the development of the crack for a given displacement in each model. In all cases, stable mode I crack initiation and propagation from the crack tip is observed.

The length scale l plays a key role in influencing crack propagation. As l increases, the crack propagates more rapidly, resulting in earlier failure. This is because the length scale in gradient plasticity theory directly affects the material's flow stress, with larger values leading to increased hardening and more localized plasticity near the crack tip. As a result, the material around the crack tip becomes more resistant to deformation, accelerating crack growth. Conversely, for smaller-length scales, the crack propagation is slower, delaying failure. This demonstrates the significant impact of the length scale parameter in gradient plasticity theory on crack growth and material failure, with larger values leading to faster crack propagation and smaller values resulting in a more gradual progression.

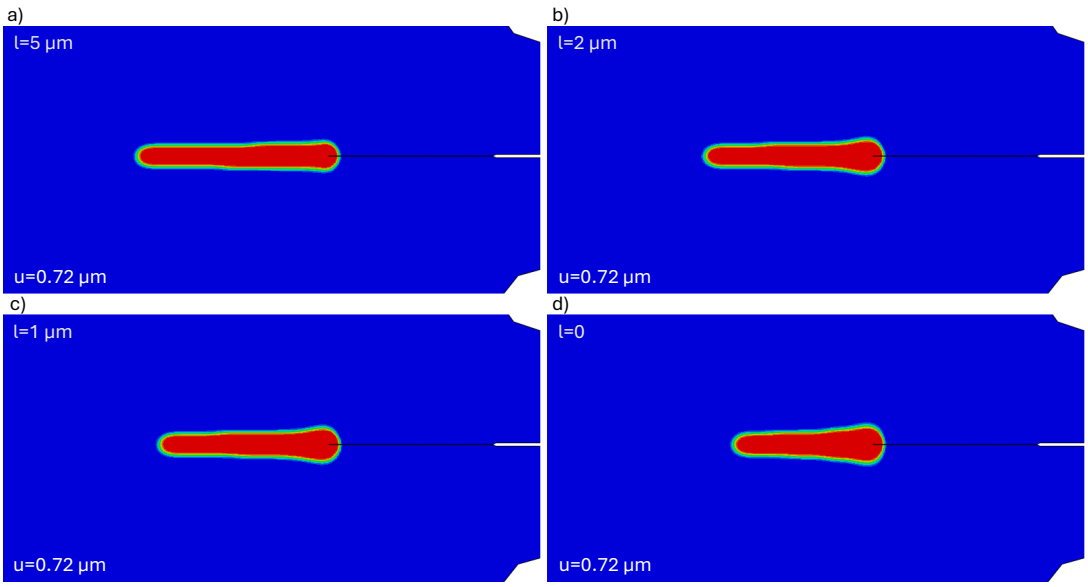

Figure 5.5: Damage contours for a given applied displacement $u = 0.72\,\mu\text{m}$ for various plastic lenght scales: a) $l = 5\,\mu\text{m}$, b) $l = 2\,\mu\text{m}$, c) $l = 1\,\mu\text{m}$, and d) $l = 0$.

Figure 5.6 shows the force-displacement curves for different values of the length scale parameter l, which governs the material's response in the context of strain gradient plasticity. For all cases, the force increases almost linearly with displacement at first, as the material deforms elastically. The force continues to rise until a peak value is reached, ranging between $4.7\,\text{kN}$ and $5.2\,\text{kN}$ depending on the length scale. After this peak, a sudden drop in force indicates the initiation and propagation of a crack.

The influence of the length scale l is particularly evident in the peak load values. As l increases, the peak load decreases, indicating that materials with larger length scales exhibit earlier crack initiation and lower maximum load-bearing capacities. This is because the larger length scale increases the stress concentration at the crack tip, as shown in the previous example, which accelerates crack formation. For example, with $l = 5.0\,\mu\text{m}$, the material reaches its peak load at a lower displacement compared to the $l = 0$ case (classical plasticity).

This trend suggests that the material's resistance to fracture decreases as the length scale increases, which reflects the inherent size-dependent hardening behavior captured by the strain gradient plasticity theory. The smaller the length scale, the more closely the material behaves like conventional plasticity, where stress gradients are

less pronounced, resulting in a higher peak load and later crack initiation.

Once the crack forms, all cases exhibit a similar post-peak behavior characterized by a rapid force drop. Suggesting that while the length scale significantly affects the onset of fracture, it has less impact on the behavior after the crack has initiated.

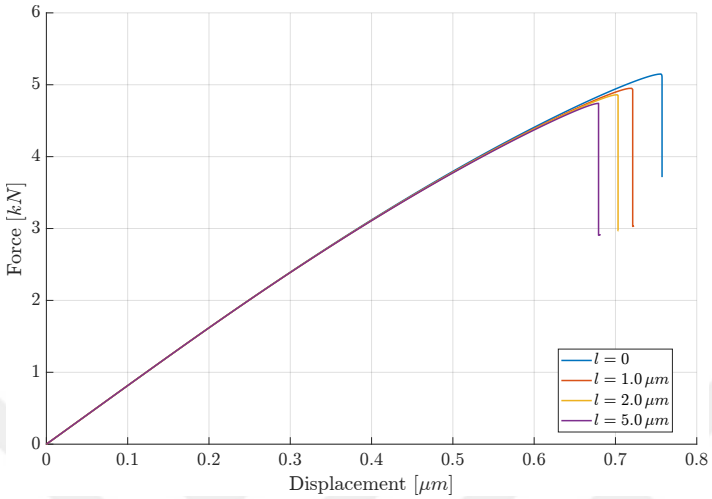

Figure 5.6: Damage contours for a given applied displacement $u = 0.72\,\mu\text{m}$ for various plastic lenght scales: a) $l = 5\,\mu\text{m}$, b) $l = 2\,\mu\text{m}$, c) $l = 1\,\mu\text{m}$, and d) $l = 0$.

Figure 5.7 illustrates the equivalent plastic strain distributions for different length scale values ($l = 0, 1, 2, 5\,\mu\text{m}$) just before crack growth begins. Across all cases, the general shape and size of the plastic zone are similar, but there are notable differences due to the influence of the strain gradient effects.

In the classical plasticity case ($l = 0$), the plastic zone is more diffused, with strain spreading over a broader region around the crack tip. This diffusion results in less localized plastic deformation, which delays the onset of crack growth. In contrast, the strain gradient plasticity solutions (with $l = 1, 2, 5\,\mu\text{m}$) exhibit more localized plastic zones. As the length scale l increases, the plastic strain becomes more concentrated near the crack tip, resulting in a sharper and more defined plastic zone. This concentration of plastic strain leads to higher stress levels at the crack tip, which accelerates crack initiation.

The effect of the length scale is evident when comparing the classical plasticity solution to the gradient-enhanced models. As l increases, the plastic zone becomes more

compact, which enhances the material's hardening response due to strain gradients, making the crack tip more prone to failure. This localization helps in triggering earlier crack formation and propagation in the gradient plasticity models compared to the classical approach.

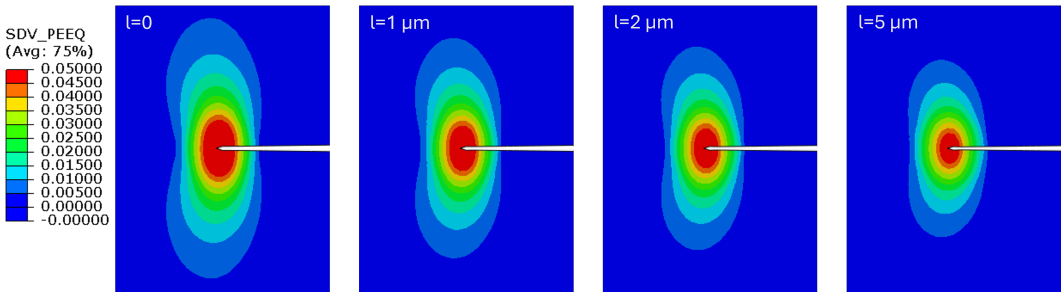

Figure 5.7: Equivalent plastic strain distributions for all lenght scales before the onset of the crack growth.

5.3 Analysis of Asymmetric Double Notch Specimen

The capabilities of the current framework are further examined by simulating mixed-mode fracture and crack coalescence in a micro-sized asymmetric double-notch specimen. The geometry, dimensions, boundary conditions, and mesh are depicted in Figure 5.8. The model assumes plane strain conditions to reflect the behavior of the specimen under loading.

The specimen is discretized using approximately 6,500 quadrilateral plane-strain elements (CPE4), with mesh refinement around the notch areas to accurately capture the stress and strain gradients. The minimum element size near the notches is set to $\Delta x = 0.2\,\mu\mathrm{m}$, ensuring sufficient resolution for analyzing the highly localized deformation near the crack tips.

The boundary conditions involve a uniform displacement applied to the top edge, inducing tension in the specimen while the bottom edge is fixed. This setup is intended to replicate mixed-mode loading, where the specimen is subjected to both mode I (opening) and mode II (shearing) loading conditions. Such loading promotes the interaction and coalescence of the cracks originating from the notches, making this geometry an ideal test case for evaluating the predictive capabilities of the strain

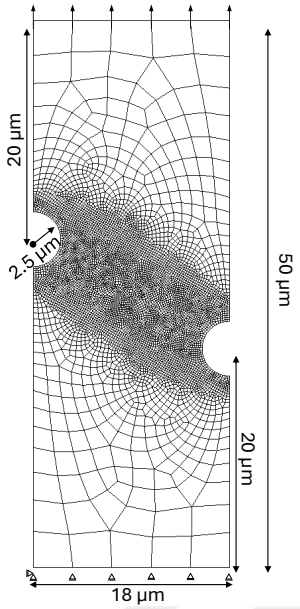

Figure 5.8: Geometry, loading configuration and mesh of the asymmetric double-notch specimen.

gradient plasticity model.

The material properties used in this study are as follows: Young's modulus $E = 78\,\mathrm{GPa}$, Poisson's ratio $\nu = 0.3$, initial yield stress $\sigma_Y = 345\,\mathrm{MPa}$, and a power law hardening exponent $N = 0.1$. The nonlocal regularization length scale is set to $L = 8\,\mu\mathrm{m}$, which is four times the critical element length, and the critical strain at which damage accumulation begins is $\varepsilon_c = 0.25$.

Similar to the compact tension example, three different intrinsic length scales ($l = 1, 2, 5\,\mu\mathrm{m}$) are analyzed in conjunction with the classical plasticity model ($l = 0$). Figure 5.9 shows the damage contours for both classical plasticity and gradient plasticity cases at different applied displacements ($u = 0.40\,\mu\mathrm{m}$, $u = 0.50\,\mu\mathrm{m}$, and $u = 0.80\,\mu\mathrm{m}$).

From the figure, it can be observed that in all cases, the damage initiates near the notches and eventually leads to the coalescence of two cracks. Initially, cracks form at the notch tips due to localized plastic deformation, and as the applied displacement increases, these cracks rapidly grow and merge. This behavior is consistent across all cases, regardless of the length scale.

However, one notable difference is the effect of the length scale parameter on crack initiation. Contrary to the compact tension example, where increasing the length scale accelerated crack formation, in this case, increasing l actually retards crack initiation. This phenomenon can be attributed to the nature of the problem being driven by plastic localization rather than the presence of a sharp crack. In the compact tension specimen, high-strain gradients developed due to the sharp crack tip, which facilitated crack growth. Here, with the blunt notch geometry, the strain gradients are less pronounced, and therefore, the presence of strain gradients delays the plastic localization process, making crack initiation more gradual as the length scale increases.

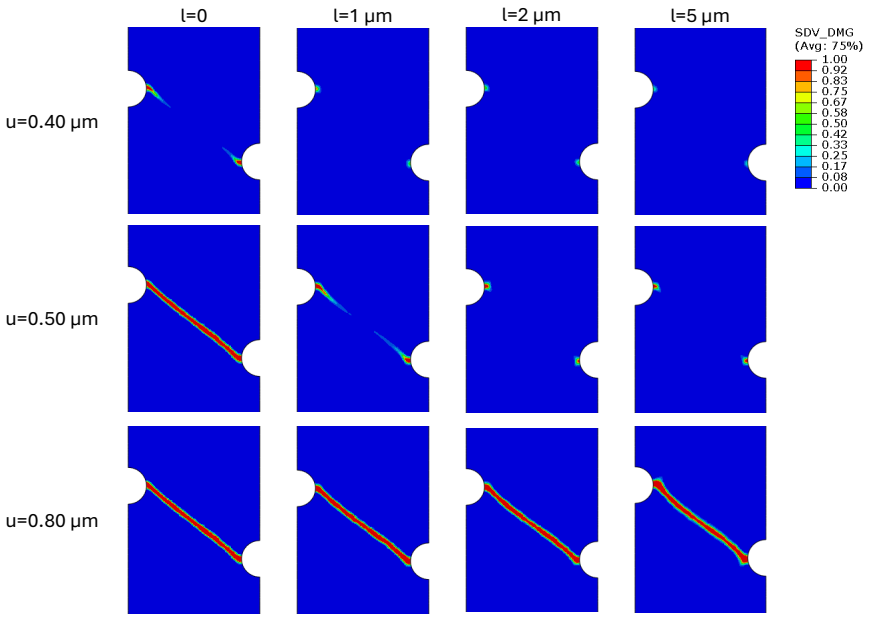

Figure 5.9: Damage contours for classical plasticity ($l = 0$) and strain gradient plasticity models ($l = 1, 2, 5\,\mu\text{m}$) at different applied displacements ($u = 0.40\,\mu\text{m}$, $u = 0.50\,\mu\text{m}$, and $u = 0.80\,\mu\text{m}$).

This trend is even more pronounced when examining the force-displacement curves shown in Figure 5.10. As the length scale parameter l increases, both the displacement at failure and the peak load capacity increase significantly. The larger the length scale, the more the material resists crack initiation, resulting in a higher peak load. This is a direct consequence of the strain gradient plasticity theory, where larger length scales contribute to additional hardening in the vicinity of the location where crack formation occurs.

For all cases, a sudden and sharp drop in force is observed immediately after reaching the peak load, similar to what was seen in previous examples. This sharp decline indicates the rapid crack propagation once the material's load-bearing capacity has been exceeded. Notably, this behavior confirms that after the peak load, gradient effects become negligible, as the strain gradient effects primarily influence the material's hardening behavior up to the point of failure. Once the crack initiates, the material behaves similarly to a classical plasticity model with rapid degradation of load capacity.

Another important observation is that while increasing the length scale delays the onset of failure and enhances the peak load, all cases ultimately experience catastrophic failure immediately after the peak. This suggests that the strain gradient effects play a significant role in delaying the initiation of cracks and influencing pre-peak behavior, but once the material reaches its load-bearing limit, the crack propagation is swift and unaffected by the length scale parameter.

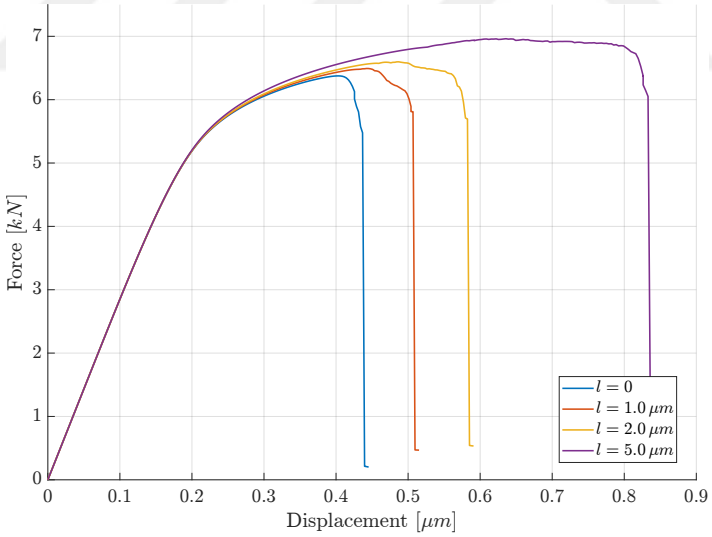

Figure 5.10: Force-displacement curves for asymmetric double-notch specimen. Classical plasticity ($l = 0$) and strain gradient plasticity models ($l = 1, 2, 5\,\mu\text{m}$) solutions.

5.4 Summary

In summary, when dealing with nonlocal damage coupled with gradient plasticity, the effect of the internal length scale parameter l is not always straightforward to predict. The role of l can vary significantly depending on the nature of the problem. In cases involving sharp cracks, defects, or notches, the length scale can act as a stress intensifier, leading to earlier crack initiation. On the other hand, in problems dominated by strain localization or gradual damage accumulation, l can diffuse stress, thereby delaying the onset of cracking. This dual nature of the length scale parameter highlights its versatility and the importance of understanding the underlying mechanics of the problem being analyzed.

CHAPTER 6

CONCLUSIONS

In this thesis, a lower-order strain gradient plasticity model has been implemented in the finite element solver ABAQUS. Two methods were employed to compute the effective plastic strain gradient, η^p: the interpolation method and the extrapolation method. The interpolation method relies solely on the plastic strain values at the integration points, while the extrapolation method calculates strain gradients using nodal values of plastic strain. Both methods were implemented for two-dimensional and three-dimensional settings.

For the extrapolation method, a nodal averaging technique is necessary to ensure a consistent distribution of plastic strain across the model, requiring additional subroutines and additional information describing the nodal connectivity. In contrast, the interpolation method offers a simpler implementation since it only uses integration point values, eliminating the need for nodal averaging. The differences between these two methods were evaluated across a variety of boundary value problems. The results demonstrate that the extrapolation method consistently predicts higher plastic strain gradients, leading to a stronger material response. However, both methods captured similar overall trends throughout the problems studied. Notably, in problems involving sharp boundaries or interactions between dissimilar materials, the extrapolation method was able to capture highly localized areas of strain gradient development, whereas the interpolation method struggled with this aspect. For problems without such geometric or material-related complexities, both methods performed comparably well.

The strain gradient framework was further extended to incorporate nonlocal damage effects. A volumetric averaging scheme was applied for nonlocal regularization, with

equivalent plastic strain chosen as the damage-driving variable. The nonlocality is governed by an additional length scale parameter, L, controlling the extent of the damage zone. In the extended CMSG theory with nonlocal damage, two length scale parameters were incorporated: the plastic length scale, l, which governs size effects and material hardening through the flow stress, and the damage length scale, L, which influences the localization and smearing of damage. With the addition of damage, a competing mechanism emerges: the hardening effect from the strain gradient theory interacts with the softening effect from the damage model. To further explore this interplay, numerical simulations were conducted to assess the effects of these length scale parameters. The influence of the damage length scale L is straightforward: larger values result in more diffused damage zones, and it was confirmed that for converged results, the length scale should be at least four times the element size near the damaged area. The role of the plastic length scale l, however, depends on the nature of the problem. For example, increasing l in problems involving sharp cracks and small-scale yielding accelerates failure. In these cases, extreme strain gradients develop at the crack tip, intensifying stress concentrations and promoting earlier crack growth. Conversely, for problems involving blunt cracks, where failure is driven by plastic flow localization, increasing l delays failure. Here, the strain gradients work to diffuse the localization of plasticity, thereby postponing fracture.

Overall, this framework captures the varying mechanisms driving material failure, depending on the geometry and loading conditions. The incorporation of both plastic and damage length scales offers a versatile approach to modeling size-dependent material behavior, damage initiation, accumulation, and crack evolution.

While this study has demonstrated the effectiveness of the lower-order strain gradient plasticity model and its extension to nonlocal damage, several areas of improvement and further exploration remain. One important direction for future work is the application of the current framework to more realistic material properties to better align the simulations with experimental observations. Incorporating experimentally derived material parameters—such as those obtained from micro-scale testing of metals, composites, or other materials—would allow for a more direct and accurate comparison between the numerical results and experimental data. This could further validate the framework's ability to capture complex material behavior and confirm its predic-

tive accuracy. Additionally, the model could be tested under various geometries and boundary conditions to explore its adaptability and performance in different structural configurations. Applying the model to more complex loading conditions, such as cyclic or multi-axial loading, would also provide deeper insights into its behavior under diverse scenarios.

REFERENCES

[1] N. Fleck and J. Hutchinson, "Strain gradient plasticity," *Advances in Applied Mechanics*, vol. 33, pp. 295–361, 1997.

[2] D. Liu, Y. He, D. J. Dunstan, B. Zhang, Z. Gan, P. Hu, and H. Ding, "Toward a further understanding of size effects in the torsion of thin metal wires: An experimental and theoretical assessment," *International Journal of Plasticity*, vol. 41, pp. 30–52, 2013.

[3] D. Liu, Y. He, D. J. Dunstan, B. Zhang, Z. Gan, P. Hu, and H. Ding, "Anomalous plasticity in the cyclic torsion of micron scale metallic wires," *Phys. Rev. Lett.*, vol. 110, p. 244301, 2013.

[4] W. Poole, M. Ashby, and N. Fleck, "Micro-hardness of annealed and work-hardened copper polycrystals," *Scripta Materialia*, vol. 34, no. 4, pp. 559–564, 1996.

[5] N. Stelmashenko, M. Walls, L. Brown, and Y. Milman, "Microindentations on W and Mo oriented single crystals: An stm study," *Acta Metallurgica et Materialia*, vol. 41, no. 10, pp. 2855–2865, 1993.

[6] D. González, J. Alkorta, J. Martínez-Esnaola, and J. Gil Sevillano, "Numerical analysis of the indentation size effect using a strain gradient crystal plasticity model," *Computational Materials Science*, vol. 82, pp. 314–319, 2014.

[7] W. D. Nix and H. Gao, "Indentation size effects in crystalline materials: A law for strain gradient plasticity," *Journal of the Mechanics and Physics of Solids*, vol. 46, no. 3, pp. 411–425, 1998.

[8] Q. Ma and D. R. Clarke, "Size dependent hardness of silver single crystals," *Journal of Materials Research*, vol. 10, no. 3, pp. 853–863, 1995.

[9] J. Stölken and A. Evans, "A microbend test method for measuring the plasticity length scale," *Acta Materialia*, vol. 46, no. 14, pp. 5109–5115, 1998.

[10] B. Ehrler, X. Hou, T. Zhu, K. P'ng, C. Walker, A. Bushby, and D. Dunstan, "Grain size and sample size interact to determine strength in a soft metal," *Philosophical Magazine*, vol. 88, no. 25, pp. 3043–3050, 2008.

[11] D. J. Lloyd, "Particle reinforced aluminium and magnesium matrix composites," *International Materials Reviews*, vol. 39, no. 1, pp. 1–23, 1994.

[12] M. Kouzeli and A. Mortensen, "Size dependent strengthening in particle reinforced aluminium," *Acta Materialia*, vol. 50, no. 1, pp. 39–51, 2002.

[13] B. Liu, W. Huang, H. Wang, M. Wang, and X. Li, "Study on the load partition behaviors of high particle content B4C/Al composites in compression," *Journal of Composite Materials*, vol. 48, no. 3, pp. 355–364, 2014.

[14] Y. Yan, L. Geng, and A. Li, "Experimental and numerical studies of the effect of particle size on the deformation behavior of the metal matrix composites," *Materials Science and Engineering: A*, vol. 448, no. 1, pp. 315–325, 2007.

[15] S. Sajjadi, H. Ezatpour, and H. Beygi, "Microstructure and mechanical properties of Al-Al2O3 micro and nano composites fabricated by stir casting," *Materials Science and Engineering: A*, vol. 528, no. 29, pp. 8765–8771, 2011.

[16] M. F. Ashby, "The deformation of plastically non-homogeneous materials," *The Philosophical Magazine: A Journal of Theoretical Experimental and Applied Physics*, vol. 21, no. 170, pp. 399–424, 1970.

[17] J. Nye, "Some geometrical relations in dislocated crystals," *Acta Metallurgica*, vol. 1, no. 2, pp. 153–162, 1953.

[18] H. Gao, Y. Huang, W. Nix, and J. Hutchinson, "Mechanism-based strain gradient plasticity— I. Theory," *Journal of the Mechanics and Physics of Solids*, vol. 47, no. 6, pp. 1239–1263, 1999.

[19] Y. Huang, H. Gao, W. Nix, and J. Hutchinson, "Mechanism-based strain gradient plasticity—II. Analysis," *Journal of the Mechanics and Physics of Solids*, vol. 48, no. 1, pp. 99–128, 2000.

[20] T. Yalcinkaya, W. Brekelmans, and M. Geers, "Deformation patterning driven

by rate dependent non-convex strain gradient plasticity," *Journal of the Mechanics and Physics of Solids*, vol. 59, no. 1, pp. 1–17, 2011.

[21] T. Yalçinkaya, W. Brekelmans, and M. Geers, "Non-convex rate dependent strain gradient crystal plasticity and deformation patterning," *International Journal of Solids and Structures*, vol. 49, no. 18, pp. 2625–2636, 2012.

[22] S. Guha, S. Sangal, and S. Basu, "Finite element studies on indentation size effect using a higher order strain gradient theory," *International Journal of Solids and Structures*, vol. 50, no. 6, pp. 863–875, 2013.

[23] E. C. Aifantis, "On the microstructural origin of certain inelastic models," *Journal of Engineering Materials and Technology*, vol. 106, no. 4, pp. 326–330, 1984.

[24] A. Acharya and J. L. Bassani, "On non-local flow theories that preserve the classical structure of incremental boundary value problems," in *IUTAM Symposium on Micromechanics of Plasticity and Damage of Multiphase Materials* (A. Pineau and A. Zaoui, eds.), (Dordrecht), pp. 3–9, Springer Netherlands, 1996.

[25] S. Chen and T. Wang, "A new hardening law for strain gradient plasticity," *Acta Materialia*, vol. 48, no. 16, pp. 3997–4005, 2000.

[26] S. Chen and T. Wang, "A new deformation theory with strain gradient effects," *International Journal of Plasticity*, vol. 18, no. 8, pp. 971–995, 2002.

[27] Y. Huang, S. Qu, K. Hwang, M. Li, and H. Gao, "A conventional theory of mechanism-based strain gradient plasticity," *International Journal of Plasticity*, vol. 20, no. 4, pp. 753–782, 2004.

[28] G. Hu, X. Liu, and T. J. Lu, "A variational method for non-linear micropolar composites," *Mechanics of Materials*, vol. 37, no. 4, pp. 407–425, 2005.

[29] R. K. Abu Al-Rub and G. Z. Voyiadjis, "A physically based gradient plasticity theory," *International Journal of Plasticity*, vol. 22, no. 4, pp. 654–684, 2006.

[30] A. Acharya and A. Beaudoin, "Grain-size effect in viscoplastic polycrystals

at moderate strains," *Journal of the Mechanics and Physics of Solids*, vol. 48, no. 10, pp. 2213–2230, 2000.

[31] N. Fleck, G. Muller, M. Ashby, and J. Hutchinson, "Strain gradient plasticity: Theory and experiment," *Acta Metallurgica et Materialia*, vol. 42, no. 2, pp. 475–487, 1994.

[32] H. Gao and Y. Huang, "Taylor-based nonlocal theory of plasticity," *International Journal of Solids and Structures*, vol. 38, no. 15, pp. 2615–2637, 2001.

[33] L. Bardella and A. Panteghini, "Modelling the torsion of thin metal wires by distortion gradient plasticity," *Journal of the Mechanics and Physics of Solids*, vol. 78, pp. 467–492, 2015.

[34] S. Chen, L. Liu, and T. Wang, "Small scale, grain size and substrate effects in nano-indentation experiment of film–substrate systems," *International Journal of Solids and Structures*, vol. 44, no. 13, pp. 4492–4504, 2007.

[35] Z. Ma, Y. Zhou, S. Long, and C. Lu, "On the intrinsic hardness of a metallic film/substrate system: Indentation size and substrate effects," *International Journal of Plasticity*, vol. 34, pp. 1–11, 2012.

[36] B. Liu, X. Qiu, Y. Huang, K. Hwang, M. Li, and C. Liu, "The size effect on void growth in ductile materials," *Journal of the Mechanics and Physics of Solids*, vol. 51, no. 7, pp. 1171–1187, 2003.

[37] J. Wen, Y. Huang, K. Hwang, C. Liu, and M. Li, "The modified Gurson model accounting for the void size effect," *International Journal of Plasticity*, vol. 21, no. 2, pp. 381–395, 2005.

[38] V. Monchiet and G. Bonnet, "A Gurson-type model accounting for void size effects," *International Journal of Solids and Structures*, vol. 50, no. 2, pp. 320–327, 2013.

[39] W. Yueguang, "Particulate size effects in the particle-reinforced metal-matrix composites," *Acta Mechanica Sinica*, vol. 17, pp. 45–58, Feb 2001.

[40] S. H. Chen and T. C. Wang, "Size effects in the particle-reinforced metal-matrix composites," *Acta Mechanica*, vol. 157, pp. 113–127, Mar 2002.

[41] D.-M. Duan, N. Q. Wu, M. Zhao, W. S. Slaughter, and S. X. Mao, "Effect of strain gradients and heterogeneity on flow strength of particle reinforced metal-matrix composites," *Journal of Engineering Materials and Technology*, vol. 124, pp. 167–173, 03 2002.

[42] Z. Xue, Y. Huang, and M. Li, "Particle size effect in metallic materials: a study by the theory of mechanism-based strain gradient plasticity," *Acta Materialia*, vol. 50, no. 1, pp. 149–160, 2002.

[43] F. Xun, G. Hu, and Z. Huang, "Size-dependence of overall in-plane plasticity for fiber composites," *International Journal of Solids and Structures*, vol. 41, no. 16, pp. 4713–4730, 2004.

[44] M. Huang and Z. Li, "Size effects on stress concentration induced by a prolate ellipsoidal particle and void nucleation mechanism," *International Journal of Plasticity*, vol. 21, no. 8, pp. 1568–1590, 2005.

[45] R. Azizi, B. Nyvang Legarth, and C. F. Niordson, "A new macroscopically anisotropic pressure dependent yield function for metal matrix composite based on strain gradient plasticity for the microstructure," *Journal of the Mechanics and Physics of Solids*, vol. 61, no. 4, pp. 991–1009, 2013.

[46] B. N. Legarth, "Plasticity dependent damage evolution in composites with strain-gradient effects," *International Journal of Solids and Structures*, vol. 63, pp. 1–10, 2015.

[47] C. F. Niordson and J. W. Hutchinson, "Non-uniform plastic deformation of micron scale objects," *International Journal for Numerical Methods in Engineering*, vol. 56, no. 7, pp. 961–975, 2003.

[48] K. Chen, W. J. Meng, F. Mei, J. Hiller, and D. J. Miller, "From micro- to nano-scale molding of metals: Size effect during molding of single crystal al with rectangular strip punches," *Acta Materialia*, vol. 59, pp. 1112–1120, 2011.

[49] B. Lu and W. J. Meng, "Roll molding of microchannel arrays on al and cu sheet metals: A method for high-throughput manufacturing," *Journal of Micro and Nano-Manufacturing*, vol. 2, pp. 1–9, 2014.

[50] C. J. Campbell and S. P. Gill, “An analytical model for the flat punch indentation size effect,” *International Journal of Solids and Structures*, vol. 171, pp. 81–91, 2019.

[51] X. Gao, H. Wang, G. Zhu, Z. Chang, N. Guo, Z. Wang, and L. Zhu, “Mechanical and fatigue properties of micro-groove structure formed by multi-pass rolling,” *Journal of the Brazilian Society of Mechanical Sciences and Engineering*, vol. 44, pp. 1–12, 2022.

[52] I. E. Unsal, E. Günay, and T. Yalcinkaya, “Local and nonlocal strain gradient approaches for size-dependent plastic deformation,” *Materials Research Proceedings*, vol. 28, pp. 1453–1462, 2024.

[53] I. E. Ünsal and T. Yalçinkaya, “Strain gradient plasticity analysis of amorphous plasticity,” *Procedia Structural Integrity*, vol. 61, pp. 164–170, 2024.

[54] B. Klusemann and S. Bargmann, “Modeling and simulation of size effects in metallic glasses with a nonlocal continuum mechanics theory,” *Journal of the Mechanical Behavior of Materials*, vol. 22, no. 1-2, pp. 51–66, 2013.

[55] Z. Xia and J. W. Hutchinson, “Crack tip fields in strain gradient plasticity,” *Journal of the Mechanics and Physics of Solids*, vol. 44, no. 10, pp. 1621–1648, 1996.

[56] S. Chen and T. Wang, “Finite element solutions for plane strain mode I crack with strain gradient effects,” *International Journal of Solids and Structures*, vol. 39, no. 5, pp. 1241–1257, 2002.

[57] M. Huang, J. Tong, and Z. Li, “A study of fatigue crack tip characteristics using discrete dislocation dynamics,” *International Journal of Plasticity*, vol. 54, pp. 229–246, 2014.

[58] E. Martínez-Pañeda and C. Betegón, “Modeling damage and fracture within strain-gradient plasticity,” *International Journal of Solids and Structures*, vol. 59, pp. 208–215, 2015.

[59] E. Martínez-Pañeda and C. Niordson, “On fracture in finite strain gradient plasticity,” *International Journal of Plasticity*, vol. 80, pp. 154–167, 2016.

[60] V. Smyshlyaev and N. Fleck, "The role of strain gradients in the grain size effect for polycrystals," *Journal of the Mechanics and Physics of Solids*, vol. 44, no. 4, pp. 465–495, 1996.

[61] B. Wu, L. Liang, H. Ma, and Y. Wei, "A trans-scale model for size effects and intergranular fracture in nanocrystalline and ultra-fine polycrystalline metals," *Computational Materials Science*, vol. 57, pp. 2–7, 2012.

[62] X. Xiao, D. Song, J. Xue, H. Chu, and H. Duan, "A size-dependent tensorial plasticity model for FCC single crystal with irradiation," *International Journal of Plasticity*, vol. 65, pp. 152–167, 2015.

[63] J. Lemaitre, *A course on damage mechanics*. Springer science & business media, 1992.

[64] A. Molinari, C. Musquar, and G. Sutter, "Adiabatic shear banding in high speed machining of Ti–6Al–4V: experiments and modeling," *International Journal of Plasticity*, vol. 18, pp. 443–459, 4 2002.

[65] U. S. Dixit, S. N. Joshi, and J. P. Davim, "Incorporation of material behavior in modeling of metal forming and machining processes: A review," *Materials & Design*, vol. 32, pp. 3655–3670, 8 2011.

[66] G. G. Ye, Y. Chen, S. F. Xue, and L. H. Dai, "Critical cutting speed for onset of serrated chip flow in high speed machining," *International Journal of Machine Tools and Manufacture*, vol. 86, pp. 18–33, 11 2014.

[67] S. Lee, J. Hwang, M. R. Shankar, S. Chandrasekar, and W. Dale Compton, "Large strain deformation field in machining," *Metallurgical and Materials Transactions A*, vol. 37, pp. 1633–1643, May 2006.

[68] M. Calamaz, D. Coupard, and F. Girot, "A new material model for 2D numerical simulation of serrated chip formation when machining titanium alloy Ti–6Al–4V," *International Journal of Machine Tools and Manufacture*, vol. 48, pp. 275–288, 3 2008.

[69] G. List, G. Sutter, X. F. Bi, A. Molinari, and A. Bouthiche, "Strain, strain rate and velocity fields determination at very high cutting speed," *Journal of Materials Processing Technology*, vol. 213, pp. 693–699, 5 2013.

[70] H. M. Zbib and E. C. Aifantis, "On the gradient-dependent theory of plasticity and shear banding," *Acta Mechanica*, vol. 92, pp. 209–225, Mar 1992.

[71] R. Engelen, N. Fleck, R. Peerlings, and M. Geers, "An evaluation of higher-order plasticity theories for predicting size effects and localisation," *International Journal of Solids and Structures*, vol. 43, no. 7, pp. 1857–1877, 2006.

[72] U. Borg, "Strain gradient crystal plasticity effects on flow localization," *International Journal of Plasticity*, vol. 23, no. 8, pp. 1400–1416, 2007.

[73] S. Chen, B. Feng, Y. Wei, and T. Wang, "Prediction of the initial thickness of shear band localization based on a reduced strain gradient theory," *International Journal of Solids and Structures*, vol. 48, no. 21, pp. 3099–3111, 2011.

[74] C. Zhu, T. Harrington, V. Livescu, G. T. Gray, and K. S. Vecchio, "Determination of geometrically necessary dislocations in large shear strain localization in aluminum," *Acta Materialia*, vol. 118, pp. 383–394, 2016.

[75] R. De Borst and H.-B. Mühlhaus, "Gradient-dependent plasticity: Formulation and algorithmic aspects," *International Journal for Numerical Methods in Engineering*, vol. 35, no. 3, pp. 521–539, 1992.

[76] A. Benallal, T. Berstad, T. Børvik, and O. S. Hopperstad, "Uniqueness, loss of ellipticity and localization for the time-discretized, rate-dependent boundary value problem with softening," *International Journal for Numerical Methods in Engineering*, vol. 84, no. 7, pp. 864–882, 2010.

[77] B. Wcisło, J. Pamin, K. Kowalczyk-Gajewska, and A. Menzel, "Numerical analysis of ellipticity condition for large strain plasticity," *AIP Conference Proceedings*, vol. 1922, p. 140008, 01 2018.

[78] M. Jirásek and S. Rolshoven, "Localization properties of strain-softening gradient plasticity models. part I: Strain-gradient theories," *International Journal of Solids and Structures*, vol. 46, no. 11, pp. 2225–2238, 2009.

[79] R. A. Toupin, "Elastic materials with couple-stresses," *Archive for Rational Mechanics and Analysis*, vol. 11, pp. 385–414, Jan 1962.

[80] R. D. Mindlin, "Micro-structure in linear elasticity," *Archive for Rational Mechanics and Analysis*, vol. 16, pp. 51–78, Jan 1964.

[81] R. Chambon, D. Caillerie, and N. El Hassan, "One-dimensional localisation studied with a second grade model," *European Journal of Mechanics - A/Solids*, vol. 17, no. 4, pp. 637–656, 1998.

[82] X. Qiu, Y. Huang, Y. Wei, H. Gao, and K. Hwang, "The flow theory of mechanism-based strain gradient plasticity," *Mechanics of Materials*, vol. 35, no. 3, pp. 245–258, 2003.

[83] G. Pijaudier-Cabot and Z. P. Bažant, "Nonlocal damage theory," *Journal of engineering mechanics*, vol. 113, no. 10, pp. 1512–1533, 1987.

[84] R. H. J. Peerlings, R. De Borst, W. A. M. Brekelmans, and J. H. P. De Vree, "Gradient enhanced damage for quasi-brittle materials," *International Journal for Numerical Methods in Engineering*, vol. 39, no. 19, pp. 3391–3403, 1996.

[85] M. Geers, R. de Borst, and R. Peerlings, "Damage and crack modeling in single-edge and double-edge notched concrete beams," *Engineering Fracture Mechanics*, vol. 65, no. 2, pp. 247–261, 2000.

[86] B. Tatli, C. Erdoğan, M. E. Özcan, and T. Yalçinkaya, "Phase field fracture modelling of crack initiation and propagation in dual-phase microstructures," *Procedia Structural Integrity*, vol. 61, pp. 12–19, 2024.

[87] O. Bulut, C. Erdogan, and T. Yalçinkaya, "Dwell fatigue fracture in ti microstructures through crystal plasticity and phase field fracture frameworks," *Procedia Structural Integrity*, vol. 61, pp. 3–11, 2024.

[88] S. Waseem, İzzet Erkin Ünsal, and T. Yalçinkaya, "Phase field modelling of fatigue crack growth at constant and variable amplitude loading," *Procedia Structural Integrity*, vol. 42, pp. 1692–1699, 2022.

[89] S. Waseem, C. Erdogan, and T. Yalçinkaya, "Phase field modeling of fatigue crack growth retardation under single cycle overloads," *International Journal of Fatigue*, vol. 179, p. 108064, 2024.

[90] J. Mediavilla, R. Peerlings, and M. Geers, "An integrated continuous–discontinuous approach towards damage engineering in sheet metal forming processes," *Engineering Fracture Mechanics*, vol. 73, no. 7, pp. 895–916, 2006.

[91] J. Mediavilla, R. H. J. Peerlings, and M. G. D. Geers, "Discrete crack modelling of ductile fracture driven by non-local softening plasticity," *International Journal for Numerical Methods in Engineering*, vol. 66, no. 4, pp. 661–688, 2006.

[92] A. Seupel, G. Hütter, and M. Kuna, "An efficient FE-implementation of implicit gradient-enhanced damage models to simulate ductile failure," *Engineering Fracture Mechanics*, vol. 199, pp. 41–60, 2018.

[93] A. L. Gurson, "Continuum theory of ductile rupture by void nucleation and growth: Part i—yield criteria and flow rules for porous ductile media," *Journal of Engineering Materials and Technology*, vol. 99, pp. 2–15, 01 1977.

[94] V. Tvergaard, "Influence of voids on shear band instabilities under plane strain conditions," *International Journal of Fracture*, vol. 17, pp. 389–407, Aug 1981.

[95] V. Tvergaard and A. Needleman, "Analysis of the cup-cone fracture in a round tensile bar," *Acta Metallurgica*, vol. 32, no. 1, pp. 157–169, 1984.

[96] S. Bergo, D. Morin, and O. S. Hopperstad, "Numerical implementation of a non-local GTN model for explicit FE simulation of ductile damage and fracture," *International Journal of Solids and Structures*, vol. 219-220, pp. 134–150, 2021.

[97] S. Rolshoven, *Nonlocal plasticity models for localized failure*. PhD thesis, EPFL, Lausanne, 2003.

[98] J. Chen, *A nonlocal damage model for elasto-plastic materials based on gradient plasticity theory*. PhD thesis, ETH Zurich, Zürich, 2001.

[99] K. Saanouni and M. Hamed, "Micromorphic approach for finite gradient-elastoplasticity fully coupled with ductile damage: Formulation and computa-

tional aspects," *International Journal of Solids and Structures*, vol. 50, no. 14, pp. 2289–2309, 2013.

[100] G. D. Nguyen, A. M. Korsunsky, and J. P.-H. Belnoue, "A nonlocal coupled damage-plasticity model for the analysis of ductile failure," *International Journal of Plasticity*, vol. 64, pp. 56–75, 2015.

[101] T. Brepols, S. Wulfinghoff, and S. Reese, "Gradient-extended two-surface damage-plasticity: Micromorphic formulation and numerical aspects," *International Journal of Plasticity*, vol. 97, pp. 64–106, 2017.

[102] G. Z. Voyiadjis and R. K. A. Al-Rub, "Gradient plasticity theory with a variable length scale parameter," *International Journal of Solids and Structures*, vol. 42, no. 14, pp. 3998–4029, 2005.

[103] J. Liu and T. ElSayed, "A strain gradient plasticity theory with application to wire torsion," *International Journal of Damage Mechanics*, vol. 24, no. 4, pp. 512–528, 2015.

[104] H. Ban, Y. Yao, S. Chen, and D. Fang, "The coupling effect of size and damage in micro-scale metallic materials," *International Journal of Plasticity*, vol. 95, pp. 251–263, 2017.

[105] G. I. Taylor, "The mechanism of plastic deformation of crystals. part I.—theoretical," *Proceedings of the Royal Society of London. Series A, Containing Papers of a Mathematical and Physical Character*, vol. 145, no. 855, pp. 362–387, 1934.

[106] A. Arsenlis and D. Parks, "Crystallographic aspects of geometrically-necessary and statistically-stored dislocation density," *Acta Materialia*, vol. 47, no. 5, pp. 1597–1611, 1999.

[107] J. Bishop and R. Hill, "A theoretical derivation of the plastic properties of a polycrystalline face-centred metal," *The London, Edinburgh, and Dublin Philosophical Magazine and Journal of Science*, vol. 42, no. 334, pp. 1298–1307, 1951.

[108] J. Bishop and R. Hill, "A theory of the plastic distortion of a polycrystalline aggregate under combined stresses.," *The London, Edinburgh, and Dublin Philosophical Magazine and Journal of Science*, vol. 42, no. 327, pp. 414–427, 1951.

[109] U. F. Kocks, "The relation between polycrystal deformation and single-crystal deformation," *Metallurgical Transactions*, vol. 1, no. 5, pp. 1121–1143, 1970.

[110] R. Asaro and A. Needleman, "Overview no. 42 texture development and strain hardening in rate dependent polycrystals," *Acta Metallurgica*, vol. 33, no. 6, pp. 923–953, 1985.

[111] D. Peirce, R. Asaro, and A. Needleman, "Material rate dependence and localized deformation in crystalline solids," *Acta Metallurgica*, vol. 31, no. 12, pp. 1951–1976, 1983.

[112] J. W. Hutchinson and R. Hill, "Bounds and self-consistent estimates for creep of polycrystalline materials," *Proceedings of the Royal Society of London. A. Mathematical and Physical Sciences*, vol. 348, no. 1652, pp. 101–127, 1976.

[113] S. Kok, A. Beaudoin, and D. Tortorelli, "A polycrystal plasticity model based on the mechanical threshold," *International Journal of Plasticity*, vol. 18, no. 5, pp. 715–741, 2002.

[114] L. Evers, D. Parks, W. Brekelmans, and M. Geers, "Crystal plasticity model with enhanced hardening by geometrically necessary dislocation accumulation," *Journal of the Mechanics and Physics of Solids*, vol. 50, no. 11, pp. 2403–2424, 2002.

[115] Y. Huang, L. Zhang, T. Guo, and K.-C. Hwang, "Mixed mode near-tip fields for cracks in materials with strain-gradient effects," *Journal of the Mechanics and Physics of Solids*, vol. 45, no. 3, pp. 439–465, 1997.

[116] C.-W. Nan and D. Clarke, "The influence of particle size and particle fracture on the elastic/plastic deformation of metal matrix composites," *Acta Materialia*, vol. 44, no. 9, pp. 3801–3811, 1996.

[117] M. Jirásek and S. Rolshoven, "Comparison of integral-type nonlocal plasticity models for strain-softening materials," *International Journal of Engineering Science*, vol. 41, no. 13, pp. 1553–1602, 2003.

[118] V. Tvergaard and A. Needleman, "Effects of nonlocal damage in porous plastic solids," *International Journal of Solids and Structures*, vol. 32, no. 8, pp. 1063–1077, 1995.

[119] T. Linse, G. Hütter, and M. Kuna, "Simulation of crack propagation using a gradient-enriched ductile damage model based on dilatational strain," *Engineering Fracture Mechanics*, vol. 95, pp. 13–28, 2012.

[120] M. Samal, M. Seidenfuss, and E. Roos, "A new mesh-independent Rousselier's damage model: Finite element implementation and experimental verification," *International Journal of Mechanical Sciences*, vol. 51, no. 8, pp. 619–630, 2009.

[121] D. Sornin and K. Saanouni, "About elastoplastic nonlocal formulations with damage gradients," *International Journal of Damage Mechanics*, vol. 20, no. 6, pp. 845–875, 2011.

[122] M. G. D. Geers, R. L. J. M. Ubachs, and R. A. B. Engelen, "Strongly nonlocal gradient-enhanced finite strain elastoplasticity," *International Journal for Numerical Methods in Engineering*, vol. 56, no. 14, pp. 2039–2068, 2003.

[123] S. Qu, Y. Huang, H. Jiang, C. Liu, P. D. Wu, and K. C. Hwang, "Fracture analysis in the conventional theory of mechanism-based strain gradient (CMSG) plasticity," *International Journal of Fracture*, vol. 129, Oct 2004.